GEOSPHERE

GEOSPHERE; v. 16, no. 1

https://doi.org/10.1130/GES02102.1

12 figures; 4 tables; 1 set of supplemental files

CORRESPONDENCE: trehu@coas.oregonstate.edu

CITATION: Tréhu, A.M., de Moor, A., Mieres Madrid, J., Sáez, M., Chadwell, C.D., Ortega-Culaciati, F., Ruiz, J., Ruiz, S., and Tryon, M.D., 2020, Post-seismic response of the outer accretionary prism after the 2010 Maule earthquake, Chile: Geosphere, v. 16, no. 1, p. 13–32, https://doi.org/10.1130/GES02102.1.

Science Editor: Shanaka de Silva
Guest Associate Editor: Laura M. Wallace

Received 10 December 2018
Revision received 10 August 2019
Accepted 14 October 2019

Published online 11 December 2019

Post-seismic response of the outer accretionary prism after the 2010 Maule earthquake, Chile

Anne M. Tréhu[1], Alexander de Moor[1,*], José Mieres Madrid[2], Miguel Sáez[2], C. David Chadwell[3], Francisco Ortega-Culaciati[2], Javier Ruiz[2], Sergio Ruiz[2], and Michael D. Tryon[3,†]

[1]College of Earth Ocean and Atmospheric Sciences, Oregon State University, Corvallis, Oregon 97331, USA
[2]Department of Geophysics, University of Chile, Santiago, Chile
[3]Marine Physical Lab, Scripps Institution of Oceanography, La Jolla, California 92093, USA

ABSTRACT

To investigate the dynamic response of the outer accretionary prism updip from the patch of greatest slip during the 2010 M_w 8.8 Maule earthquake (Chile), 10 ocean-bottom seismometers (OBSs) were deployed from May 2012 to March 2013 in a small network with an inter-instrument spacing of 7–10 km. Nine were recovered, with four recording data from intermediate-band three-component seismometers and differential pressure gauges, and five recording data from absolute pressure gauges (APGs). All instruments were also equipped with fluid flow meters designed to detect very low rates of flow into or out of the seafloor. We present hypocenters for local earthquakes that have S-P times <17 s (i.e., within ~125 km of the network), with a focus on events located beneath or near the network. Most of the seismicity occurred either near the boundary between the active accretionary prism and continental basement or in the outer rise seaward of the trench. For many outer-rise earthquakes, the P and S arrivals are followed by a distinctive T-phase arrival. Very few earthquakes, and none located with hypocenters deemed "reliable," were located within the active accretionary prism or on the underlying plate boundary. Nonvolcanic tremor-like pulses and seafloor pressure transients (but no very-low-frequency earthquakes or fluid flow) were also detected. Many of the tremor observations are likely T-phases or reverberations due to soft seafloor sediments, although at least one episode may have originated within the accretionary prism south of the network. The transient seafloor pressure changes were observed simultaneously on three APGs located over the transition from the active prism to the continental basement and show polarity changes over short distances, suggesting a shallow source. Their duration of several hours to days is shorter than most geodetic transients observed using onshore GPS networks. The results demonstrate the need for densely spaced and large-aperture OBS networks equipped with APGs for understanding subduction zone behavior.

INTRODUCTION

On 27 February 2010, a M_w 8.8 megathrust earthquake ruptured the central Chilean margin. This event, termed the Maule earthquake, filled a well-documented seismic gap that had not ruptured in a major earthquake since 1835 (Campos et al., 2002; Lomnitz, 2004; Ruegg et al., 2009; Ruiz and Madariaga, 2018). A large number of slip models have been published for this event based on seismic, geodetic, satellite, and tsunami data (e.g., Moreno et al., 2010; Lay et al., 2010; Delouis et al., 2010; Tong et al., 2010; Lorito et al., 2011; Vigny et al., 2011; Lin et al., 2013;Yue et al., 2014). While the models differ in their details, a common feature of most of the models is that the patch of greatest slip occurred to the northwest of the epicenter (Fig. 1). Still debated, however, are the cross-strike location of greatest slip, the relationship between slip in the main shock and aftershock activity, and whether slip propagated to the trench or was arrested when it reached the accretionary prism, which is thought to be ~30 km wide in this region. Resolution of these questions is important for understanding the conditions under which coseismic slip can propagate beneath or through the accretionary wedge and the implications for tsunamigenesis.

Until the 2011 Tohoku earthquake (Japan), slip during megathrust earthquakes was generally not expected to propagate to the deformation front because of the assumed velocity-strengthening rheology of the trench sediments that are accreted to form the outer accretionary wedge (Lallemand et al., 1994; Wang and Hu, 2006), with the exception being rare "tsunami" earthquakes characterized by slow, shallow slip and generation of a tsunami much larger than expected based on the radiated seismic energy (for a review, see Ye et al. [2016]). The M_w 9.0 Tohoku earthquake, however, indicated that under some conditions, the outer accretionary wedge can lurch seaward by tens of meters (Sato et al., 2011; Kodaira et al., 2012). Assuming that subduction is driven primarily by slab pull, the accretionary prism would be in the stress shadow generated by a locked segment of the plate boundary and would therefore appear to be locked prior to an earthquake (Wang and Dixon, 2004). For this reason, it is difficult to anticipate whether seismogenic slip is likely to extend to the trench or be arrested as it reaches the accretionary prism based on preseismic observations. In the latter case, stress would increase in the accretionary prism

*Now at Canyonlands Field Institute, Moab, Utah 84532, USA
†Retired

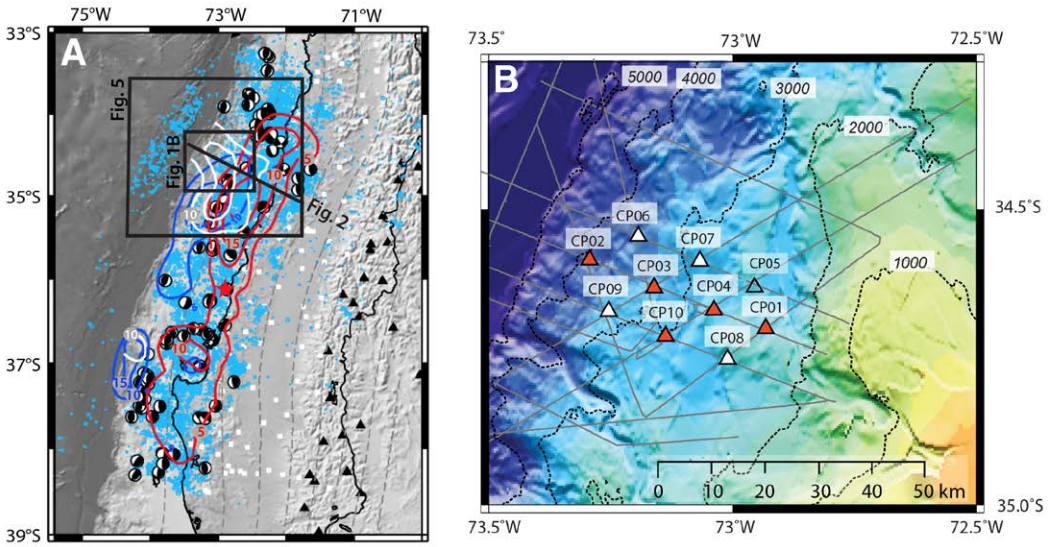

Figure 1. (A) Map showing several representative slip models for the 2010 Mw 8.8 Maule earthquake (Chile) and aftershock distribution. (Modified from Figure 1 of Rietbrock et al. (2012) to add the slip model of Yue et al. (2014) and the location of the maps in Figures 1B and 5 and the cross-section of Figure 2.) Slip models: 5, 10, and 15 m slip contours from Lorito et al. (2011) in red; 10 and 15 m slip contours from Vigny et al. (2011) in blue; 10 and 15 m slip from Yue et al. (2014) in white. Red star is the main shock epicenter. Light blue dots are aftershock epicenters. Source mechanisms of selected aftershocks are also shown. White squares are seismic stations deployed onshore for the international aftershock monitoring network known as IMAD. Black triangles are volcanos. Black lines represent the coastline of Chile and its border with Argentina. Grey dashed lines are contours to the plate boundary at 20 km intervals from model Slab1.0 of Hayes et al. (2012). (B) Location of the ChilePEPPER network overlain on bathymetry. Red triangles show locations of absolute pressure gauges (APG); white triangles are intermediate-band three-component seismometers and differential pressure gauges (DPG). Open triangle (site CP05) indicates a site where the instrument package was not recovered, although it was still responding to acoustic release commands when the site was revisited in February 2017 during cruise MGL1701 of RV *Marcus Langseth* (nearly 4 yr after the initial recovery attempt). Data from sites CP02 and CP03 were sensitive to seismic frequencies for only 10 and 100 days after deployment, respectively, because of instrument malfunction. Grey lines are high-resolution multichannel seismic reflection lines collected during R/V *Melville* cruise MV1206. Background bathymetry (contoured in meters) is from Global Multi-Resolution Topography (Ryan et al., 2009).

immediately after the earthquake and would be relaxed through postseismic creep on the plate boundary and within the prism. Few in situ observations are available of this process because, with the exception of the continental margin offshore Japan (Nakano et al., 2016), most subduction zones are not adequately instrumented to detect slow slip, nonvolcanic tremor, and other subtle clues to the postseismic response of the outer accretionary prism.

The aftershocks in the months immediately after the Maule earthquake (Fig. 1A) were recorded on a dense network of temporary seismic stations, known as IMAD (International Maule Aftershock Deployment) (e.g., Lange et al., 2012; Rietbrock et al., 2012; Hayes et al., 2013). This effort was complemented by networks of ocean-bottom seismometers (OBSs) with interstation spacing of 25 km or more to record aftershocks and provide data for improved velocity models (Lieser et al., 2014; Hicks et al., 2014). While many offshore aftershocks were observed, few were located beneath the outer accretionary wedge, and no observations of low-frequency earthquakes or nonvolcanic tremor have been reported from the OBS data. ChilePEPPER (Project Evaluating Prism Post-Earthquake Response) was designed to test the hypothesis that compressive stress in the accretionary prism increased as a result of >15 m of sudden plate boundary slip to the east and that this stress was being relaxed through internal wedge deformation, which would be expected to result in slow earthquakes, microseismicity, and fluid expulsion driven by increased pore-fluid pressure. When the project was conceived, coseismic slip models and the relatively small far-field tsunami generated by the earthquake suggested that slip had not propagated to the trench, although some subsequent work challenged that conclusion (Yue et al., 2014). To capture the dynamic response of the accretionary wedge to the expected change in stress, 10 OBSs equipped with intermediate or broadband three-component seismometers, absolute or differential pressure gauges, and chemical aqueous transport (CAT) meters (Tryon et al., 2001) were deployed updip of the patch of greatest slip in May 2012 and recorded data until March 2013. Instruments were arranged in a small-aperture network with an inter-instrument spacing of 7–10 km (Fig. 1B). High-resolution swath bathymetric (Maksymowicz et al., 2017), potential field (Maksymowicz et al., 2015), and multi-channel seismic reflection data (Tréhu and Tryon, 2012; Tréhu et al., 2019) were also acquired.

BACKGROUND

Tectonic Setting

The western boundary of the South American plate is characterized by subduction of the Nazca plate below the South American plate at the Peru-Chile trench. Historically, it is the most seismically active subduction zone in the world, nucleating events >M 8 roughly every 10 yr (Campos et al., 2002), with

three since 2010. The short seismic cycle, long historical record (Lomnitz, 2004; Ruiz and Madariaga, 2018), along-strike variability in trench sediment fill and slab dip (e.g., Contreras-Reyes and Osses, 2010), and complex topography of the incoming plate make this region a natural laboratory for understanding seismogenesis and the segmentation of plate-boundary faults. Proposed causes for seismic segmentation (i.e., zones that repeatedly rupture in earthquakes separated by zones that are frequently barriers to rupture propagation) include subducting ridges and seamounts on the incoming plate (Contreras-Reyes et al., 2010; Contreras-Reyes and Carrizo, 2011), peninsulas and bends in the coastline of the overriding plate (Loveless et al., 2010), variations in sediment subduction and thickness (Ruff, 1989; Scholl et al., 2015), and fractured zones in the incoming oceanic plate (Poli et al., 2017).

The 100 km × 500 km region that ruptured during the Maule earthquake was a well-documented, mature seismic gap that had last ruptured in a large event (M ~8.5) in 1835 (Ruegg et al., 2009). This segment, which is bounded to the south by the rupture zone of the 21 and 22 May 1960 M_w 8.0 Concepción and M_w 9.5 Valdivia earthquakes and to the north by the rupture zone of the 1985 Valparaiso earthquake, is characterized by subduction in a N78°E direction at 66 mm/yr (Angermann et al., 1999). High sedimentation rates linked to deglaciation and erosion of the Andes mountains since the Pliocene (e.g., Kukowski and Oncken, 2006; Völker et al., 2013) and blocking of sediment transport to the north by the Juan Fernández Ridge (Contreras-Reyes et al., 2010) has led to a sediment-filled trench and construction of an accretionary wedge composed primarily of terrigenous sediments with rare interbedded ash layers (Mix et al., 2003). Along-strike variability within the accretionary wedge has been attributed to episodic phases of trench sediment accretion and erosion (Bangs and Cande, 1997; Contardo et al., 2008; Contreras-Reyes et al., 2017).

Along the segment of margin where the OBS network was deployed, a 20–50-km-wide wedge with a subduction channel <1 km thick and a subduction zone backstop correlated with the slope break has been inferred based on several large-aperture seismic transects (Moscoso et al., 2011; Contreras-Reyes et al., 2017). The ChilePEPPER network straddles one of these transects (Moscoso et al., 2011). This profile has been interpreted to show an accretionary wedge defined by P-wave velocity <4.5 km/s adjacent to a paleo–accretionary complex with velocity of 4.5–6 km/s overlain by a slope basin up to 2 km thick that extends from the shelf break to the coast (Fig. 2). The solid white lines indicate the top and bottom of the subducted oceanic crust and the short-dashed white line shows the base of the continental crust interpreted from the velocity model (Moscoso et al., 2011). The long dashed line shows the interpreted boundary between the active accretionary prism and a Cretaceous paleo-accretionary complex that forms the continental backstop in this region (Contreras-Reyes et al., 2017). More regionally, a subducting seamount near the hypocenter of the

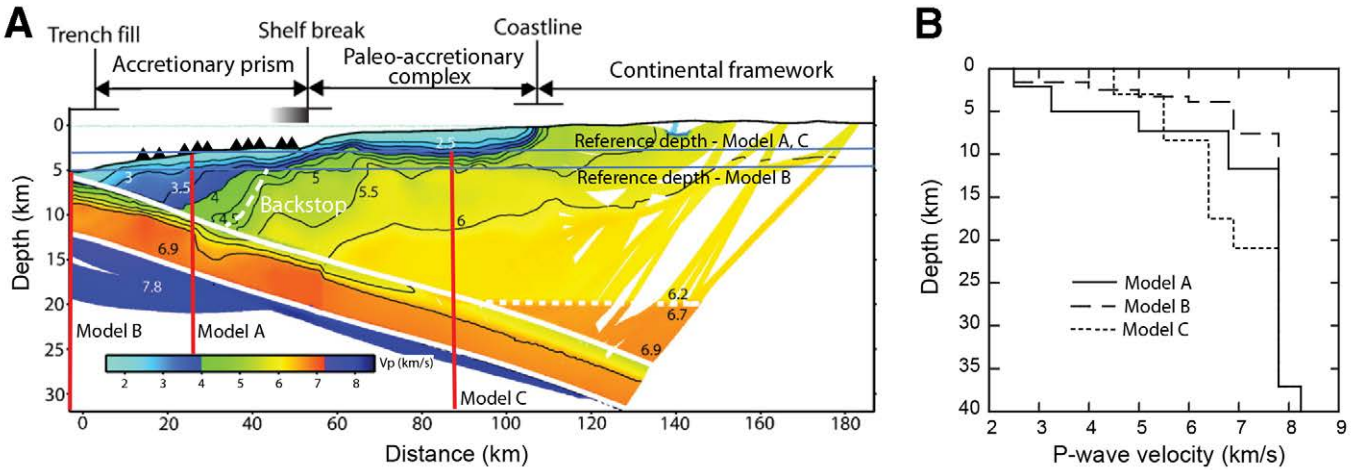

Figure 2. (A) P-wave velocity (Vp) model of Moscoso et al. (2011). Solid white lines indicate the top and bottom of the subducted oceanic crust and short-dashed white line shows the base of the continental crust interpreted from the velocity model (Moscoso et al., 2011). Velocities are in units of km/s. Depth is relative to sea level. The locations of the three velocity-depth profiles discussed in the text and shown in B are indicated by vertical red lines, and the reference depths used for locating earthquakes with these models are shown by horizontal blue lines. The boundary between active accretionary prism and the paleo-accretionary rocks that form the continental basement, which is interpreted based on the position of a strong lateral velocity gradient, is shown as a long-dash white line. Contreras-Reyes et al. (2017) interpreted this boundary to be co-located with the slope break and used the slope break as a proxy for the position of the backstop along strike. High-resolution multichannel seismic data have shown that the projection to the seafloor of this gradient is a complex zone of transpression and transtension located seaward of the slope break (Tréhu et al., 2019), indicated by the shaded rectangle shown above the cross-section. Locations of the ChilePEPPER ocean-bottom seismometers (see Fig. 1B for location) projected onto the cross-section are shown by the black triangles. (B) P-wave velocity versus depth below sea level for models A, B and C.

earthquake has been interpreted from a high P-velocity anomaly in the upper plate by Hicks et al. (2014), who speculated that this feature may have caused frictional heterogeneities on the plate interface that promoted the initial nucleation of the Maule event. Other local density and gravity anomalies have also been correlated with the patch of greatest slip, suggesting that subducting or obducted seamounts may act as asperities (Maksymowicz et al., 2015). Cubas et al. (2013a) and Maksymowicz et al. (2015) have estimated the basal friction using Coulomb wedge theory and have concluded that the frictional coefficient was lower on the patch of highest slip. Their conclusion that low basal friction is correlated with interseismic coupling and/or large coseismic slip is consistent with studies along other subduction margins (e.g., Hikurangi [New Zealand]: Fagereng, 2011; Tohoku [Japan]: Cubas et al., 2013b).

Seismological Constraints on the Maule Earthquake and Its Aftershocks

The along-strike distribution and downdip limit of slip during the M_w 8.8 Maule event are well constrained based on regional seismic, teleseismic, GPS, and interferometric synthetic-aperture radar (InSAR) data and show that the earthquake was a bilateral rupture that extended along ~500 km of the Chilean coastline, with the largest slip patches occurring to the north and south of the epicenter (e.g., Tong et al., 2010; Pollitz et al., 2011; Vigny et al., 2011; Moreno et al., 2012; Lin et al., 2013; Yue et al., 2014). The updip extent of seismogenic slip, however, varies depending on model parameterization because of limited offshore data. Even when data from offshore DART (Deep-Ocean Assessment and Reporting of Tsunamis) buoys are included in the data set used to constrain the model, different investigators obtain different solutions (Fig. 1A). For example, the model of Lin et al. (2013) suggests that coseismic slip did not propagate through the shallowest 15–20 km of the plate boundary, suggesting that the plate boundary beneath the accretionary wedge slips aseismically during the interseismic period. In contrast, Yue et al. (2014) concluded that >10 m of slip locally extended to the trench along the portion of the plate boundary updip from the patch of greatest slip. Understanding whether slip propagated to the trench is important for understanding aftershock distribution, frictional properties of the megathrust, forearc structure of the region, effects of subducting topography, and future seismic hazard assessment.

In response to the Maule event, seismologists from Chile, Europe, and the United States deployed a temporary 164-station network onshore for seven months to monitor aftershock activity (Russo et al., 2011). Several groups also deployed short-period OBSs for several months during the year following the earthquake (Lieser et al., 2014; Hicks et al. 2014). Over 100,000 aftershocks have been located and >400 focal mechanisms have been constructed from these data sets (Agurto et al., 2012; Lange et al., 2012; Rietbrock et al., 2012; Hayes et al., 2013). The OBS data have been used for joint inversion of velocity structure and seismicity (Hicks et al., 2014; Lieser et al., 2014) with a resolution controlled by the relatively sparse inter-instrument spacing of several tens of kilometers. Despite its importance for understanding plate-boundary slip, no attempts to detect nonvolcanic tremor, which is commonly interpreted to be a short-period proxy for slow slip, have been reported from these offshore data.

Aftershock seismicity from Rietbrock et al. (2012) is shown in in Figure 1A. Most of the seismicity was located on or near the plate boundary between 40 and 140 km landward of the deformation front, with a second, less-continuous band of events at greater depth; most source mechanisms for earthquakes in this band indicate low-angle thrust motion on or near the plate interface. Aftershocks with normal faulting mechanisms were recorded beneath the outer rise seaward of the trench, especially along the northern end of the rupture zone. Evidence for an offshore splay fault along the northern boundary of the rupture zone was reported by Lieser et al. (2014) based on OBS data. All studies document a notable dearth of aftershock activity within or beneath the forearc within ~40 km of the trench. Rietbrock et al. (2012) interpreted this to indicate that slip models in which the largest slip magnitude is within 40 km of the trench and the highest downdip gradient in slip is correlated with greatest moment release in aftershocks were most consistent with global patterns in the relationship between slip during large earthquakes and aftershock distribution. In contrast, Lange et al. (2012) and Moscoso et al. (2011) argued that this pattern suggested that the outer forearc did not slip during the main shock and was accommodating plate motion aseismically.

INSTRUMENTATION

Ten (10) Lamont-Doherty Earth Observatory (Palisades, New York, USA) OBSs from the Ocean Bottom Seismograph Instrument Pool (OBSIP; http://www.obsip.org/) were available on short notice for ChilePEPPER (Table 1). Five OBSs (SL-OBSs) were equipped with a three-component L4C 1 Hz geophone with a low-noise amplifier and a differential pressure gauge (DPG). The other five OBSs (CI-OBSs) each contained a Trillium Compact broadband seismometer and a Paroscientific absolute pressure gauge (APG). The SL-OBSs recorded 40 samples/s (sps) and the CI-OBSs recorded 125 sps. CAT flow meters (Tryon et al., 2001), which are designed to detect flow rates of 0.01–1.5 cm/yr into or out of the seafloor, were integrated into the OBS packages by using the patch of seafloor covered by the OBS anchor as the collection area monitored by the CAT meter, which was attached to the side of the OBS and recovered with it (Tréhu and Tryon, 2012).

Nine of the 10 OBSs that were deployed in May 2012 during R/V *Melville* cruise MV1206 were recovered in March 2013 during on R/V *Point Sur* cruise PS1306. One SL-OBS (site CP05) responded to the release command but remains on the seafloor. The remaining SL-OBSs (sites CP06–CP09) generally performed well and recorded data for the entire deployment, although CP07 and CP08 had occasional artifacts that intermittently distorted the waveforms. Unfortunately, the seismometers in the CI-OBSs did not record data, so only pressure data from these instruments were used for this study (Fig 1B). Three of the APGs (at sites CP01, CP04, and CP10) recorded good-quality data for

TABLE 1. SITE LOCATIONS (SEE FIG. 1B), SAMPLE RATE, AND COMPONENTS RECORDED

Site	Latitude (S)			Longitude (W)			Water depth (m)	Sample rate (sps)	Comments
	Decimal degrees	Degrees	Minutes	Decimal degrees	Degrees	Minutes			
CP01	34.70182	34	42.1091	72.93232	72	55.9394	2395	125	APG
CP02	34.58622	34	35.1734	73.29314	73	17.5884	3924	125	APG (to 17 Aug 2012)
CP03	34.63270	34	37.9617	73.16094	73	9.6565	3272	125	APG (to 29 May 2012)
CP04	34.67109	34	40.2652	73.03790	73	2.2739	2673	125	APG
CP05	34.61964	34	37.1786	72.95682	72	57.4089	2550	40	Not recovered
CP06	34.54564	34	32.7382	73.19254	73	11.5524	3623	40	X, Y, Z, DPG
CP07	34.58792	34	35.2754	73.06748	73	4.0486	2790	40	X, Y, Z, DPG
CP08	34.75379	34	45.2271	73.00970	73	0.5817	2398	40	X, Y, Z, DPG
CP09	34.67334	34	40.4004	73.25416	73	15.2494	3224	40	X, Y, Z, DPG
CP10	34.71460	34	42.8759	73.13726	73	8.2356	2967	125	APG

Notes: X, Y, and Z refer to three orthogonal geophone components. APG—absolute pressure gauge; DPG—differential pressure gauge; sps—samples per second.

seismic frequencies <2 Hz for the entire deployment. Rapidly increasing instrument noise for frequencies >20 Hz (Webb and Nooner, 2016), however, limited the utility of the APGs for detecting local earthquakes with magnitude <~3 (Fig. 3). Unfortunately, two of the APGs lost sensitivity to seismic frequencies after ~10 and 100 days, respectively, because of internal corrosion. For more details on OBS performance, see Tréhu (2013).

Timing for the OBSs was provided by an internal clock that was calibrated to a GPS clock before deployment and after recovery, and timing was corrected assuming a linear drift rate. Total clock drift ranged from –0.87 to 1.16 s. As a secondary, qualitative check on the timing accuracy of the instruments, we looked at four large, deep teleseismic events (deMoor, 2015), two from Argentina and two from Colombia, with origin times distributed over the duration of the ChilePEPPER deployment to see whether the time lags between instruments remained constant, as they should have if they were due only to differences in local crustal structure and the distance between the source and the receiver. Deep events were chosen because of their impulsive P-wave and steep incident angles. Unfortunately, only five stations recorded all four events. Using cross-correlation of waveforms from these events, bandpass

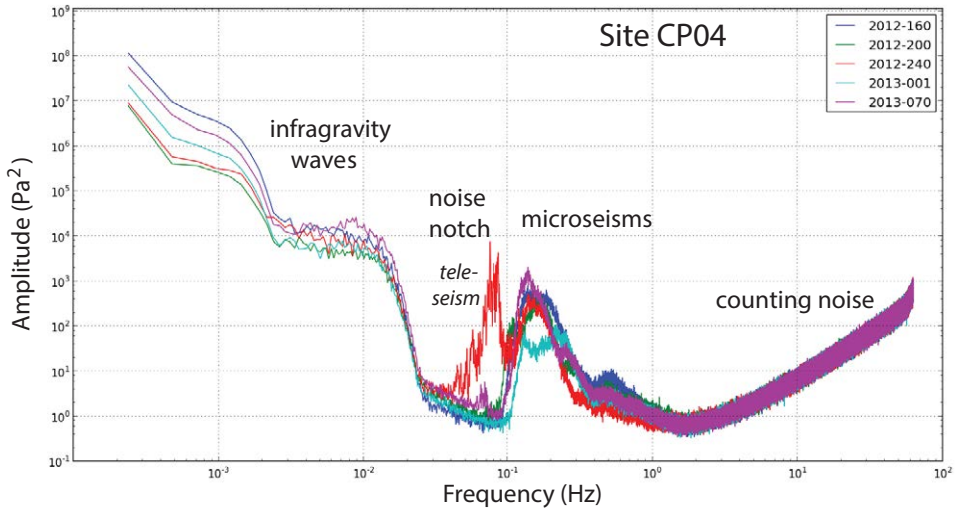

Figure 3. Power spectra of absolute pressure gauge data for day-long records at site CP04 (see Fig. 1B for location) on five different days distributed through the deployment. The legend indicates color coding by year and Julian day. Similar spectra were observed at sites CP01 and CP10. These spectra are not corrected for counting noise (Webb and Nooner, 2016).

filtered at 0.1–1 Hz, we concluded that the APG at site CP10 contained a timing error. This was confirmed by examining P-wave residuals at CP10 after initially locating earthquakes using Hypo71 software (Lee and Lahr, 1975) without including a timing correction for CP10. A decrease in the residual at CP10 with time was observed, leading to an empirical clock drift correction for CP10 of -0.004s/day and initial time offset of 1.5 s (deMoor et al., 2015). A timing correction based on this analysis was applied to picks from CP10. Average residuals for stations other than at CP10 are <0.2 s and show no systematic temporal variation throughout the deployment. Because the network was sampling a single quadrant of the radiation pattern for the direct P-wave from these deep events, these observations also served as a check on polarity. The APG data were multiplied by –1 for consistency with the seismometer data.

Figure 4A shows vertical component (BHZ) or pressure (HDH) across the network from one of the largest earthquakes to occur beneath the network and illustrates several characteristics of the data. This event is the second of a pair of approximately collocated events with M_b 4.7 and 4.5 that occurred on 15 September 2012 at 00:40 and 00:50 UTC and were reported in the U.S. Geological Survey Comprehensive Earthquake Catalog (ComCat; https://earthquake.usgs.gov/earthquakes/search). A third event from the same location with M_L 3.4 was reported by the Chilean National Seismological Center (CSN) at

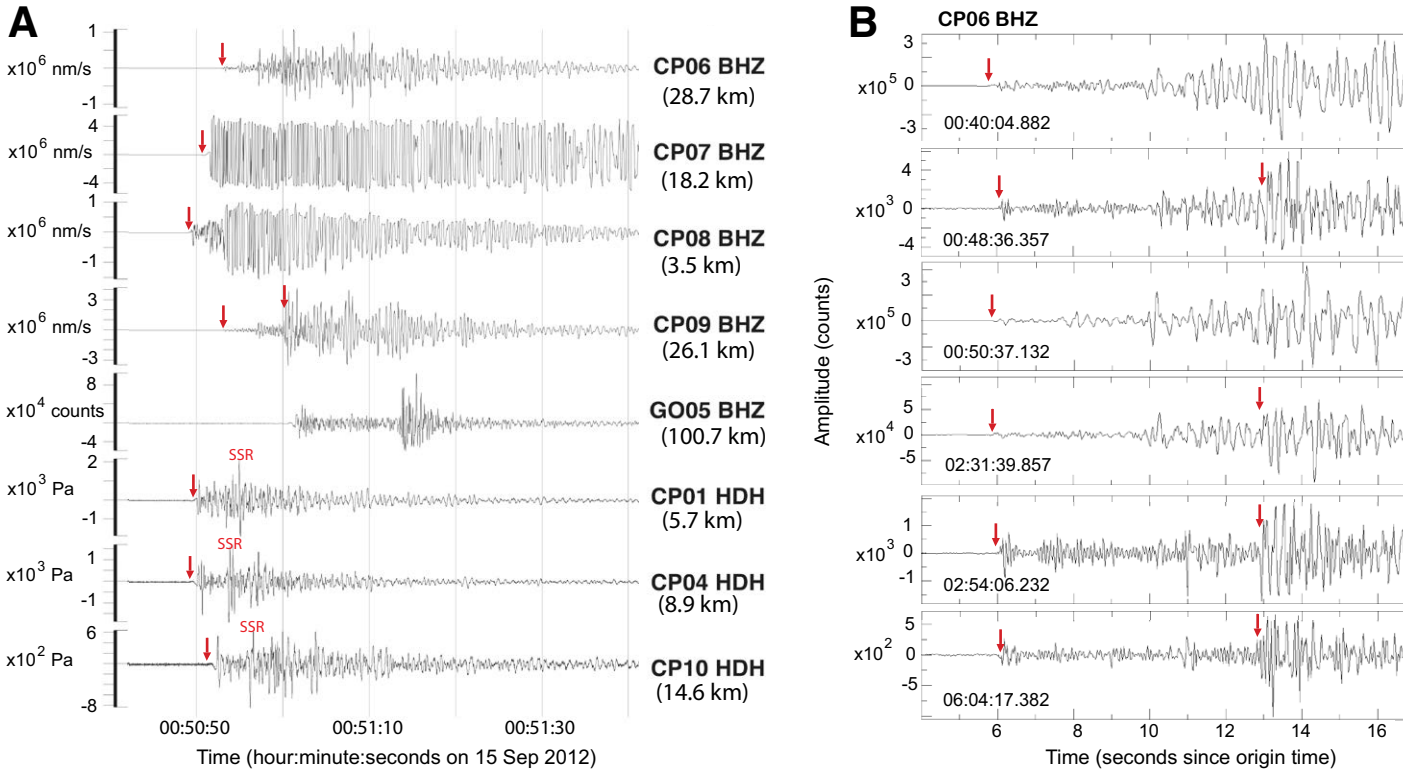

Figure 4. (A) Vertical ground velocity (BHZ) and pressure (HDH) data recorded across the ChilePEPPER network (see Fig. 1B for location) from an earthquake within the network on 15 September 2012; time is shown as hour:minute:second UTC. Source-receiver distance is indicated below the station name. Red arrows show the P- and S-wave arrival-time pick used for locations. SSR indicates the reflection of the P-wave from the sea surface above the instrument. GO05 is an onshore station (35.01°S, 71.93°S; Fig. 5A) that was not used for the catalog of Table S1 (see footnote 1) but is shown here to illustrate the difference in code length between an onshore station that is well coupled to the ground and an ocean-bottom seismometer emplaced on soft seafloor sediment. (B) Seismograms recorded at station CP06 for six approximately co-located earthquakes on 15 September 2012, showing variation in amplitude, waveform, and frequency content of events in this sequence. Data have been filtered with a passband of 1–15 Hz. P- and S-wave arrival time picks used for locations are marked by red arrows. All S-waves were picked using horizontal as well as vertical component data.

02:31. We located several additional smaller earthquakes very near these three events. Figure 4B shows the vertical component at site CP06 for several events in this sequence, including the three reported by ComCat and CSN. The two largest events were recorded across the network, but the signal was clipped on the two closest seismometers so that shear-wave arrival times could not be identified at these two sites (Fig. 4A); absolute pressure sensors at these distances (HDH) did not clip, demonstrating their ability to measure strong, high-frequency, local signals as well as very-long-period signals. On the other hand, the signal on the pressure sensors did not rise above background noise level for smaller, high-frequency earthquakes, even though these were well recorded by the seismometers. Note that the waveforms from these earthquakes at CP06 differ (Fig. 4B), indicating different fault mechanisms. The most complete data set was obtained for the event at 02:31, for which both P- and S-wave arrivals were clear on all four instruments equipped with seismometers and P-wave arrivals were clear on the three pressure sensors functioning at that time, resulting in a total of 11 travel-time picks for that event.

DATA ANALYSIS

Local Earthquakes

Hypocenters

Data were input into an Antelope database for display and phase picking. Events were detected automatically using the ratio of the long term to the short term amplitude average, but all arrival times used for locations were picked manually. The picks were then exported and reformatted for input to Hypo71 (Lee and Lahr, 1975) for calculating event locations. This classic program was used because it is well documented, flexible, and suitable for the small network aperture and relatively small number and local nature of the events being located. A one-dimensional P-wave velocity model was extracted from kilometer 28 in the model of Moscoso et al. (2011), which corresponds to the center of the ChilePEPPER network (model A in Fig. 2B). The reference depth for the top of the velocity model was placed at the mean depth of the stations (2.9 km below sea level [bsl]), and station delays or advances were defined by the difference between the reference depth and the station depth divided by the velocity of the first layer in the velocity model. This method assumes that the ray paths in layer 1 are vertical, an assumption that would be violated for very shallow, local events. Different station delays were used for P- and S-wave picks.

While P-wave velocities (Vp) for the study area are well constrained, the S-wave velocity (Vs) for the outer accretionary wedge is poorly constrained by the controlled source results. To estimate the regional Vp/Vs ratio, we located the 15 September earthquake at 02:31 for a series of Vp/Vs ratios from 1.6 to 2.6 and for hypocentral depths from 1 to 17 km relative to our reference depth of 2.87 km bsl. The minimum root mean squared (RMS) travel-time misfit for this event was for a depth of 7 km and a Vp/Vs ratio of 2.0–2.2 (Table 2, event 1). This relatively high Vp/Vs ratio is consistent with the Vp/Vs ratio for the outer accretionary wedge in this region obtained by Hicks et al. (2014) and with Vp/Vs ratios measured in cores from the Nankai accretionary wedge, Japan (Hashimoto et al., 2011). The low S-wave velocity is probably due to the presence of unconsolidated sediments in the accretionary wedge. In contrast, for an event located in the trench ~40 km west of the network, the minimum RMS travel-time residual was for a depth of 9–13 km and a Vp/Vs ratio of 1.8 (Table 2, event 2).

All events with at least five arrival-time picks and a location within ~125 km of the ChilePEPPER network (as indicated by an S-P time <17s) were identified and located (de Moor, 2015). In addition, events with only four P-wave

TABLE 2. ROOT MEAN SQUARED MISFIT AS A FUNCTION OF RATIO OF P- TO S-WAVE VELOCITY (Vp/Vs) AND SOURCE DEPTH FOR AN EVENT BENEATH THE ChilePEPPER ARRAY (EVENT 1) AND ONE LOCATED WEST OF THE ARRAY BENEATH THE OUTER RISE (EVENT 2)

Depth* (km)	Event 1 Vp/Vs					Depth* (km)	Event 2 Vp/Vs				
	1.60	1.80	2.00	2.20	2.40		1.60	1.80	2.00	2.20	2.40
1	1.21	0.62	1.00	1.00	2.38	1	1.27	1.48	1.19	1.19	1.18
3	0.59	0.52	0.66	0.66	0.95	3	1.27	1.47	1.22	1.22	1.14
5	0.59	0.56	0.46	0.46	0.72	5	1.27	1.45	1.28	1.28	1.17
7	0.55	0.47	0.44	0.44	0.80	7	0.44	1.48	1.26	1.26	1.17
9	0.58	0.48	0.50	0.50	0.71	9	0.44	0.42	1.24	1.24	1.17
11	0.58	0.52	0.51	0.51	0.79	11	0.44	0.42	1.31	1.31	1.17
13	0.58	0.52	0.50	0.50	0.90	13	0.44	0.42	0.53	0.53	1.19
15	0.58	0.53	0.58	0.58	1.02	15	0.44	0.43	0.52	0.52	1.31
17	0.59	0.55	0.50	0.50	1.15	17	0.44	0.43	0.51	0.51	1.33

*Relative to reference depth of 2.9 km below sea level.
Note: Cell outlines highlight combination of depth and Vp/Vs that minimizes the root mean squared travel-time misfit.

arrival time picks and no S-wave picks were included in our catalog if the high-frequency content of the signal suggested a nearby source. Hypocentral parameters were calculated for a starting depth of 8 km relative to the reference depth of 2.9 km below sea level. After an initial run in which all earthquakes were located using velocity model A (Fig. 2B) and a Vp/Vs ratio of 2.2, earthquakes west of –73.2° were relocated using model B (Fig. 2B) and a Vp/Vs ratio of 1.78. As an empirical test of the reliability of the hypocentral parameters, events with an RMS travel-time misfit <1.0 s and nominal horizontal errors <20 km were relocated using a starting depth of 13 km, and only events with a solution located within 15 km of the first solution were retained. This second test yielded a catalog of 453 events, including 147 events with RMS residuals <0.5 s and epicenters located within 16 km of a ChilePEPPER station. Of these, 35 were located using at least six arrival-time picks. The average RMS travel-time misfit for all events is 0.19 s; for events with at least six picks, RMS misfit is 0.22 s; for events with eight or more picks, it is 0.35 s. Coda magnitudes were estimated as described in Section S1 of the Supplemental Material[1]. The complete catalog is provided as Table S1 (footnote 1); however, actual uncertainties in the hypocentral parameters for most of the events in Table S1 are large and poorly defined, and the catalog should be used primarily as a tool to help initiate future studies.

Comparison to Other Catalogs

The distribution of epicenters in our catalog (Fig. 5A) is generally consistent with the distribution of epicenters in the ComCat catalog for the time period of the ChilePEPPER deployment (Fig. 5B), and with the catalog of Lieser et al. (2014) developed from OBS data from 20 September to 25 December 2012 (Fig. 5C). All three catalogs show a low level of seismicity beneath the outermost wedge (note that two "outer wedge" events in the ComCat catalog are likely mislocated, as discussed below). Most of the activity is focused near the boundary between the inner and outer wedge or seaward of the deformation front beneath the outer rise.

To examine possible biases in locations of offshore earthquakes located using only onshore observations, we compared hypocenters for events in the ComCat catalog that were located within or near the ChilePEPPER network (i.e., events between 34.5° and 35.0°S and between 72.8° and 73.8°W). Figure 6A suggests that ComCat epicenters may be systematically too far east and too deep along a transect perpendicular to the coast and overlying the ChilePEPPER network. A similar systematic bias has been documented for earthquakes occurring offshore central Cascadia (Pacific coast of North America) and attributed to the difference in crustal structure between the Oregon Coast

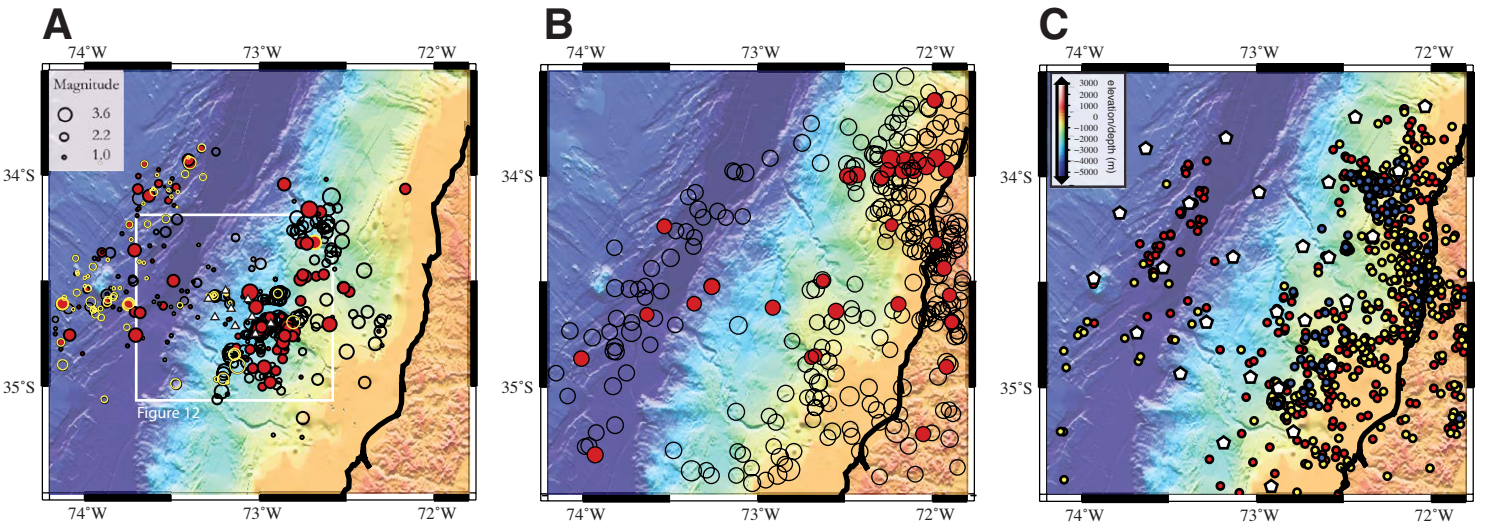

Figure 5. (A) Events located during ChilePEPPER deployment (see Fig. 1 for location) overlain on bathymetry. Open circles indicate events located using only four or five P and S-wave arrival time picks. Red filled circles indicate events located with six or more phase picks. Circle radius is determined by the local coda magnitude determined as described the Supplemental Material (see footnote 1). Yellow outlines indicate events for which a T-phase was observed. White triangles show the stations of the ChilePEPPER network. (B) Events in the U.S. Geological Survey Comprehensive Catalog (ComCat; https://earthquake.usgs.gov/earthquakes/search/) for the period during which the ChilePEPPER network was active (red filled circles) and from 1 March 2010 until the beginning of ChilePEPPER deployment (open circles). Magnitudes range from 4.1 to 5.2. (C) Events reported by Lieser et al. (2014) based an ocean-bottom seismometer (OBS) network deployed from 20 September to 25 December 2010; white hexagons are OBS locations. Events are color coded by location quality: blue—excellent; yellow—very good; red—good. The elevation/depth scale applies to all three maps.

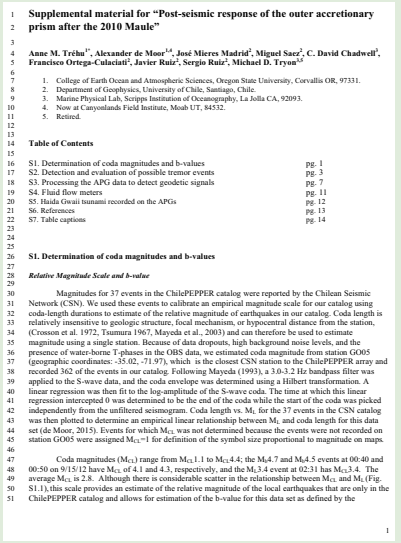

Supplemental material for "Post-seismic response of the outer accretionary prism after the 2010 Maule"

Anne M. Tréhu[1*], Alexander de Moor[1,4], José Mieres Madrid[2], Miguel Saez[2], C. David Chadwell[3], Francisco Ortega-Culaciati[2], Javier Ruiz[2], Sergio Ruiz[2], Michael D. Tryon[3,5]

1. College of Earth Ocean and Atmospheric Sciences, Oregon State University, Corvallis OR, 97331.
2. Department of Geophysics, University of Chile, Santiago, Chile.
3. Marine Physical Lab, Scripps Institution of Oceanography, La Jolla CA, 92093.
4. Now at Canyonlands Field Institute, Moab UT, 84532.
5. Retired.

Table of Contents

S1. Determination of coda magnitudes and b-values pg. 1
S2. Detection and evaluation of possible tremor events pg. 3
S3. Processing the APG data to detect geodetic signals pg. 7
S4. Fluid flow meters pg. 11
S5. Haida Gwaii tsunami recorded on the APGs pg. 12
S6. References pg. 13
S7. Table captions pg. 14

S1. Determination of coda magnitudes and b-values

Relative Magnitude Scale and b-value

Magnitudes for 37 events in the ChilePEPPER catalog were reported by the Chilean Seismic Network (CSN). We used these events to calibrate an empirical magnitude scale for our catalog using coda-length durations to estimate of the relative magnitude of earthquakes in our catalog. Coda length is relatively insensitive to geologic structure, focal mechanism, or hypocentral distance from the station, (Crosson et al. 1972, Tsumura 1967, Mayeda et al., 2003) and can therefore be used to estimate magnitude using a single station. Because of data dropouts, high background noise levels, and the presence of water-borne T-phases in the OBS data, we estimated coda magnitude from station GO05 (geographic coordinates: -35.02, -71.97), which is the closest CSN station to the ChilePEPPER array and recorded 362 of the events in our catalog. Following Mayeda (1993), a 3.0-3.2 Hz bandpass filter was applied to the S-wave data, and the coda envelope was determined using a Hilbert transformation. A linear regression was then fit to the log-amplitude of the S-wave coda. The time at which this linear regression intercepted 0 was determined to be the end of the coda while the start of the coda was picked independently from the unfiltered seismogram. Coda length vs. M_L for the 37 events in the CSN catalog was then plotted to determine an empirical linear relationship between M_L and coda length for this data set (de Moor, 2015). Events for which M_{CL} was not determined because the events were not recorded on station GO05 were assigned M_{CL}=1 for definition of the symbol size proportional to magnitude on maps.

Coda magnitudes (M_{CL}) range from M_{CL}1.1 to M_{CL}4.4; the M_L4.7 and M_L4.5 events at 00:40 and 00:50 on 9/15/12 have M_{CL} of 4.1 and 4.3, respectively, and the M_L3.4 event at 02:31 has M_{CL}3.4. The average M_{CL} is 2.8. Although there is considerable scatter in the relationship between M_{CL} and M_L (Fig. S1.1), this scale provides an estimate of the relative magnitude of the local earthquakes that are only in the ChilePEPPER catalog and allows for estimation of the b-value for this data set as defined by the

1

[1]Supplemental Material. Technical details related to determination of coda magnitudes and b-values, detection and evaluation of possible non-volcanic tremor events, and processing of absolute pressure gauge data to detect geodetic signals. Table of hypocentral parameters for the earthquakes in the ChilePEPPER catalog and a discussion of the fluid flow. Please visit https://doi.org/10.1130/GES02102.S1 or access the full-text article on www.gsapubs.org to view the Supplemental Material.

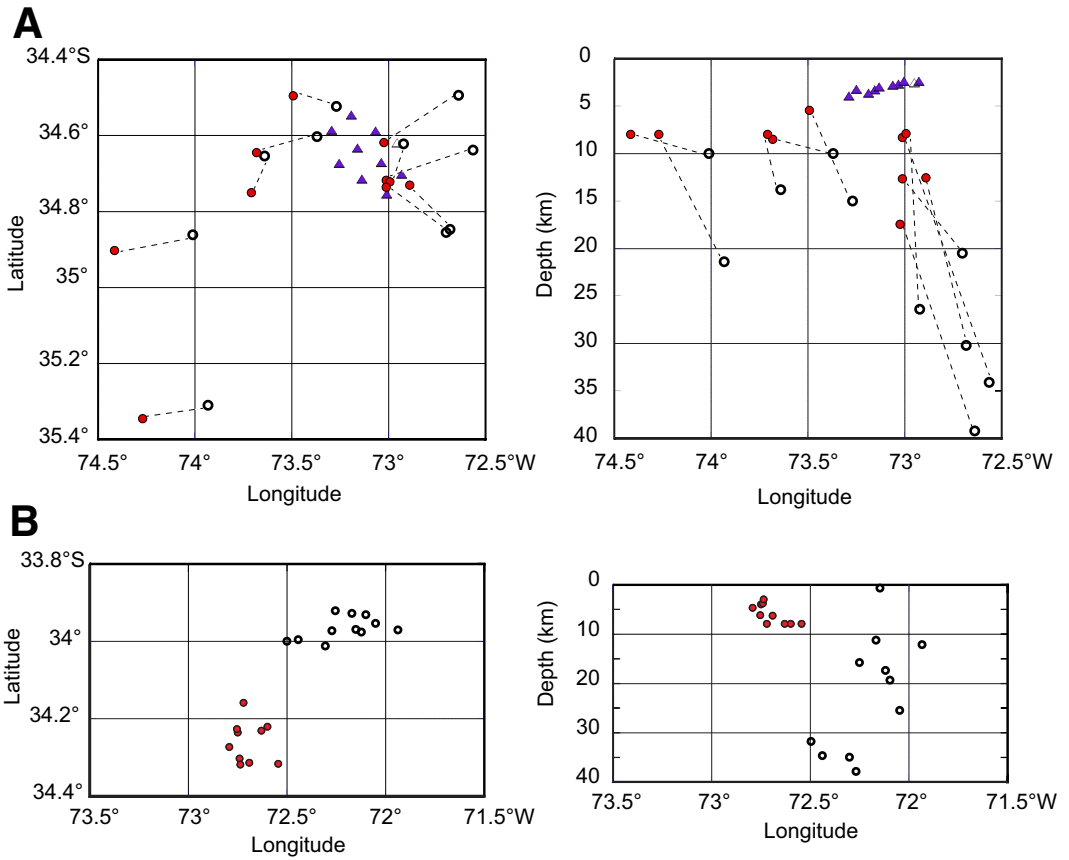

Figure 6. (A) Comparison between hypocenters reported in the U.S. Geological Survey ComCat catalog (https://earthquake.usgs.gov/earthquakes/search/) (open circles) and those determined from the ChilePEPPER network (see Fig. 1B for location) (red filled circles). Depth is relative to sea level. Purple triangles indicate the locations of ChilePEPPER instruments. Because the events do not define two distinctly different populations, a dashed line is used to connect hypocenters for the same event. (B) Same as A for events located north of the ChilePEPPER network. For reasons discussed in the text, it is likely that both sets of hypocenters have systematic biases.

Range and the continental margin as well as to the lack of close stations when only onshore data are available (Williams et al., 2011; Tréhu et al., 2015).

A cluster of relatively large-magnitude earthquakes in Figure 5A located near 34.2°S, 72.7°W corresponds to earthquakes near 34.0°S, 72.2°W in Figure 5B. Figure 6B shows the difference between ComCat hypocenters and our hypocenters for these earthquakes. The epicenters in our catalog for these events are probably systematically biased to be too close to the network because of the high Vp/Vs ratio we used for locating all events east of 73.2°W. Although a high Vp/Vs ratio is appropriate for the events originating in the wedge beneath the network, it is likely too high for events outside the network, for which the ray path is primarily in the crust and upper mantle. Depths for events in Figure 6B are poorly resolved for both catalogs. Relocation of these events in an accurate three-dimensional velocity model and using travel time observed both onshore and offshore is needed to obtain more accurate hypocentral parameters for these events. In the subsequent discussion, we focus on earthquakes located within or near the ChilePEPPER network.

Depth Uncertainty and Fault Mechanisms for Selected Earthquakes

To further examine depth resolution, three of the events that occurred on 15 September 2012 near site CP08 (Fig. 1B) were relocated for fixed depths at 2 km intervals from 2 to 30 km assuming velocity model A (Fig. 2B) and a Vp/Vs ratio of 2.2 (Fig. 7A). A similar exercise was run for two earthquakes located in the outer rise west of the deformation front assuming model B and a Vp/Vs ratio of 1.78 (Fig. 7B). The smallest RMS travel-time misfits occur for the 15 September events at ~8 km relative to sea level (compared to depths of 8.3, 7.9, and 7.2 km for these events when depth was not constrained). Although

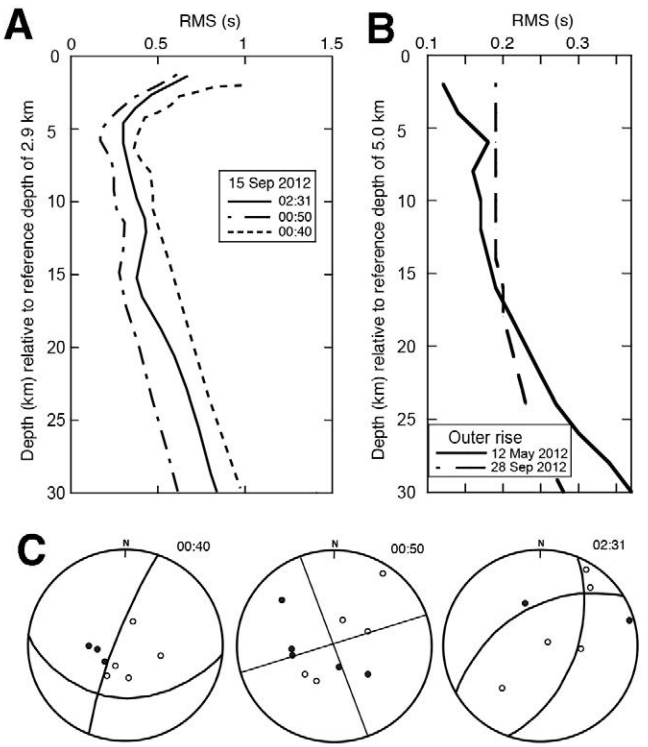

Figure 7. (A) Root mean squared (RMS) travel-time residuals as a function of source depth relative to the reference depth of 2.9 km below sea level for the three largest events on 15 September 2012 assuming velocity model A (Fig. 2). The best-recorded event was at 02:31 UTC (M_b 3.4), which was large enough to be recorded on the absolute pressure gauges and small enough to be on scale on the seismometers. The events at 00:40 (M_b 4.7) and 00:50 (M_b 4.5) were clipped on several seismometers. (B) Residuals as a function of source depth for two outer rise earthquakes located ~24 and 37 km from the closest station, assuming velocity model B. Although depth is not well resolved, the best fit is for shallow depth. (C) First-motion diagrams for three events on 15 September 2012. Lower-hemisphere projection. Filled circles are compressional first motions; open circles are dilatational first motions. Takeoff angle and azimuth were calculated for the solution in Table S1 (see footnote 1). Orthogonal nodal planes were fit by eye.

depth is not well constrained for the outer-rise earthquakes, a shallow depth is suggested.

To explore the impact of our choice of velocity model and Vp/Vs ratio, we relocated five earthquakes in the 15 September cluster for which at least six arrival time picks were available using a Vp/Vs ratio of 1.8 rather than 2.2; we also relocated these earthquakes using a P-wave model representative of the crustal structure near the coast (model C in Fig. 2; Table 3). The outer-accretionary-wedge P-wave velocity model with a Vp/Vs ratio of 2.2 yielded the shallowest source and the smallest travel-time misfit, supporting our choice of velocity model. The average horizontal and vertical uncertainties in the estimated hypocentral parameters with model A and Vp/Vs = 2.2 are 3.7 km and 3.3 km, respectively.

First-motion polarities are shown in Figure 7C for the three largest events on 15 September. Each event has a different mechanism, consistent with the observation that waveforms at a particular station differ among the events (e.g., Fig. 4B). Although the uncertainty in these mechanism estimates may be large because of the sensitivity of take-off angle and azimuth to local velocity structure, all three events are consistent with a scenario in which the greatest compressive stress is approximately horizontal and oriented NW-SE, and the intermediate and least compressive stresses are of similar magnitude.

T-Phase Observations

Nearly 50% of the events located beneath the outer rise show a distinctive T (tertiary) phase that is rarely observed for events located east of the deformation front (Fig. 8); events with T-phases are indicated in Table S1 (footnote 1) and outlined by a yellow circle in Figure 5A. T-phases are commonly observed from earthquakes originating in ocean basins and are generally thought to represent energy traveling in the SOFAR (sound fixing and ranging) channel, which occurs because the speed of sound in the ocean has a minimum at ~1000 m water depth, forming an efficient waveguide for transmitting sound in the ocean. Because of low attenuation, the T-phase may be the only phase observed for smaller events in submarine earthquake swarms (e.g., Dziak et al., 1995, 2004; Dziak, 2001; Blackman et al., 2000; Bohnenstiehl et al., 2002; Forsyth et al., 2003; Tréhu et al., 2018). They are characterized by their high-frequency content (>3 Hz), emergent nature, and a propagation velocity of 1.5 km/s. Although the mechanism for coupling P- or S-wave energy from earthquakes into the SOFAR channel remains controversial (e.g., de Groot-Hedlin and Orcutt, 2001; Balanche et al., 2009), spatial correlation of T-phase observations with outer-rise events suggests a shallow source depth (Wech et al., 2018) and/or a source where crystalline basement is at or near the seafloor for these events. That not all outer-rise events generate T-phases may indicate a range of source depths.

Possible Nonvolcanic Tremor

The importance of observations of nonvolcanic tremor as a proxy for slow slip motivated a search for tremor in the ChilePEPPER data. Wech et al. (2013) have discussed the challenges of detecting tremor from OBSs. One of the challenges is distinguishing tremor offshore from T-phases from regional or teleseismic earthquakes for which the body and surface waves are too low in amplitude or frequency to rise above the background noise level in the

TABLE 3. COMPARISON OF ROOT MEAN SQUARED (RMS) TRAVEL-TIME MISFIT AND HYPOCENTRAL DEPTH FOR VELOCITY MODELS A AND C (FIG. 2B) AND RATIOS OF P- TO S-WAVE VELOCITIES (Vp/Vs) OF 1.8 AND 2.2

15 Sep 2012	No. of picks	Model A, Vp/Vs = 1.8		Model A, Vp/Vs = 2.2		Model C, Vp/Vs = 1.8		Model C, Vp/Vs = 2.2	
(hr:min)		RMS (s)	Depth (km)	RMS (s)	Depth (km)	RMS (s)	Depth (km)	RMS (s)	Depth (km)
0:40	9	0.50	10.70	0.59	5.50	0.52	15.00	0.78	21.68
0:48	6	0.26	10.52	0.17	9.31	0.32	3.77	0.26	13.58
0:50	8	0.44	4.28	0.12	5.00	0.49	14.86	0.46	19.99
2:31	11	0.56	7.19	0.42	5.37	0.60	14.33	0.62	15.00
2:54	6	0.20	10.72	0.05	5.68	0.08	10.83	0.18	12.54
Average of five events		0.39	8.68	0.27	6.17	0.40	12.41	0.46	16.56
Depth below sea level			13.70		10.48		15.28		19.43

Notes: Depths are relative to the reference depth of 2.9 km except where indicated in the bottom row. Model A with Vp/Vs = 2.2 is the preferred model for events located beneath the network in the accretionary wedge. Time zone is UTC.

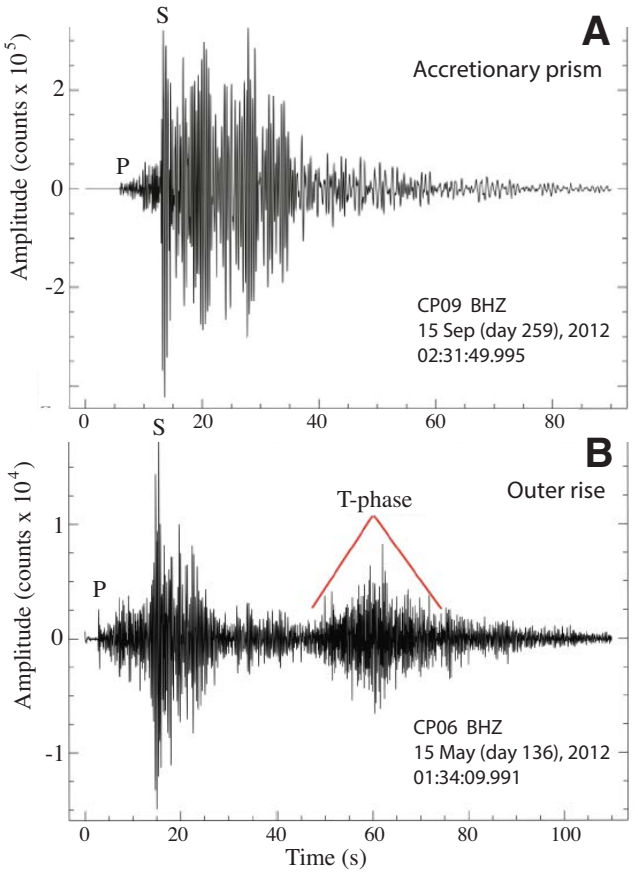

2–8 Hz passband. Because of efficient propagation of high-frequency sound in the SOFAR channel, the T-phase is sometimes the only phase observed. This phenomenon has been observed in OBS networks on the coast of Oregon (USA) for earthquakes from the Explorer Ridge (offshore British Columbia, Canada) (Czoski et al., 2012) and Blanco transform fault (offshore Oregon) (Tréhu et al., 2018). Another challenge is distinguishing tremor from the extended coda for earthquake signals recorded on seismometers emplaced on the seafloor on continental margins compared to signals recorded on well-coupled stations on land. For example, note the much longer signal recorded on the OBSs and APGs in Figure 4A compared to the signal from the same earthquake recorded onshore at station GO05.

Signals resembling nonvolcanic tremor are observed at stations CP06, CP07, and CP09 throughout the deployment. These signals were identified by bandpass filtering the data at 2–8 Hz, squaring the signal, low-pass filtering below 0.1 s and resampling at 1 sample/s, and taking the square root of this signal to produce the signal envelope. The signal envelopes from the three stations were cross-correlated using a 300 s time window with a 150 s overlap. A potential "tremor" event was detected if the maximum normalized cross-correlation between the three stations was ≥0.6. Finally, to rule out local earthquakes, the cross-correlation had to remain above 80% of its maximum value for at least 20 s. This procedure resulted in >800 events. The procedure is described in more detail in Section S2 (footnote 1), and the times and duration of tremor-like pulses detected thus are listed in Table S2. The number of tremor events per day is compared to the number of earthquakes per day in our catalog in Figure 9.

Figure 8. Examples of data recorded on the broadband vertical component (BHZ) for two typical local earthquakes. (A) An earthquake in the accretionary prism. (B) An earthquake from the outer rise, showing a distinct T-phase; P and S phases are observed for both events. The station, date (including Julian day), and time (UTC) of the first sample are shown for each event.

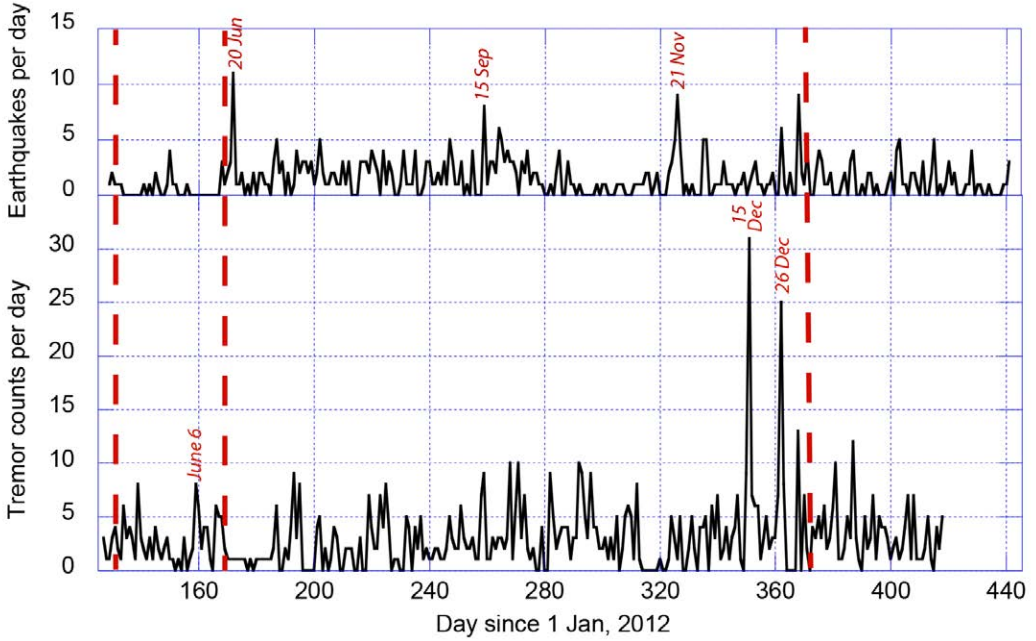

Figure 9. Comparison between the number of earthquakes per day in the catalog of Table S1 (see footnote 1) and the number of tremor events per day in the catalog of Table S2. No correlation is observed between the two catalogs. The times of the three transients observed on the absolute pressure gauges are indicated with a dashed red line.

The largest number of potential tremor events detected through this procedure occurred on 16 December 2012 (day 351 of the year 2012). Four hours of data showing possible nonvolcanic tremor (Fig. 10A) are compared to a typical 4 h window of data, which contains local and regional earthquakes (Fig. 10B). Although tremor-like signals were coherent across the ChilePEPPER network on 16 December, no such signals were recorded onshore at station GO05 (Fig. 10A), suggesting an offshore source. This is in marked contrast to tremor-like signals observed following a M_w 6.0 earthquake on 6 June that was located ~270 km southeast of the network (Fig. S2.2 [footnote 1]). For 6 June, the tremor-like signals are closely correlated with aftershock and other local earthquake activity recorded at GO05 (Fig. S2.3).

Time lags between stations picked from cross-correlations were used to try to locate the source of the tremor pulses using several techniques used to locate tremor onshore. In general, apparent tremor sources could not be localized. Lags calculated for several time windows during the 16 December tremor "swarm," however, allow us to place some constraints on the source location. Figures 10C and 10D show that cross-correlation lags are similar regardless of whether a single pulse or multiple pulses are included in the analysis, indicating that the tremor pulses on this day were coming from the same source. Picks at station CP07 are advanced relative to those at station CP09, whereas those at station CP06 are delayed. Picking the delay time for CP06 is complicated by the asymmetric nature of the cross-correlation. The peak lag is ~15 s, which implies a velocity of no more than 1 km/s to cover the 15 km distance between CP09 and CP06. However, if the lag is measured from the midpoint of the cross-correlation pulse, the lag is decreased to ~8 s, implying a velocity of at most 1.88 km/s. Picking the advance for CP07 is complicated by the double pulse of the cross-correlation. The advance of the first peak is too large for any reasonable velocity. The second peak is advanced by 5.5–6 s, implying a maximum velocity of 3.5 km/s. One reason for the asymmetric lags between tremor pulses recorded on different OBSs may be variable OBS-seafloor coupling resonances due to the relatively massive instrument packages deployed on seafloor sediment with very low shear modulus (e.g., Tréhu, 1985). The peak frequency of the signal observed on the OBSs is systematically different on different instruments (~4.5 Hz at CP06, ~3 Hz at CP09, and no distinct peak at CP07). This is likely a site rather than a source characteristic and may affect the accuracy with which lag times between events can be measured. Although the uncertainties in the lag times preclude a precise location, they are compatible with a source at a distance of a few tens of kilometers to the south or southeast of the network and with a path either in the ocean or in the shallow accretionary prism.

Although we cannot conclusively rule out a source in the water, the apparent source location landward of the deformation front for the 16 December

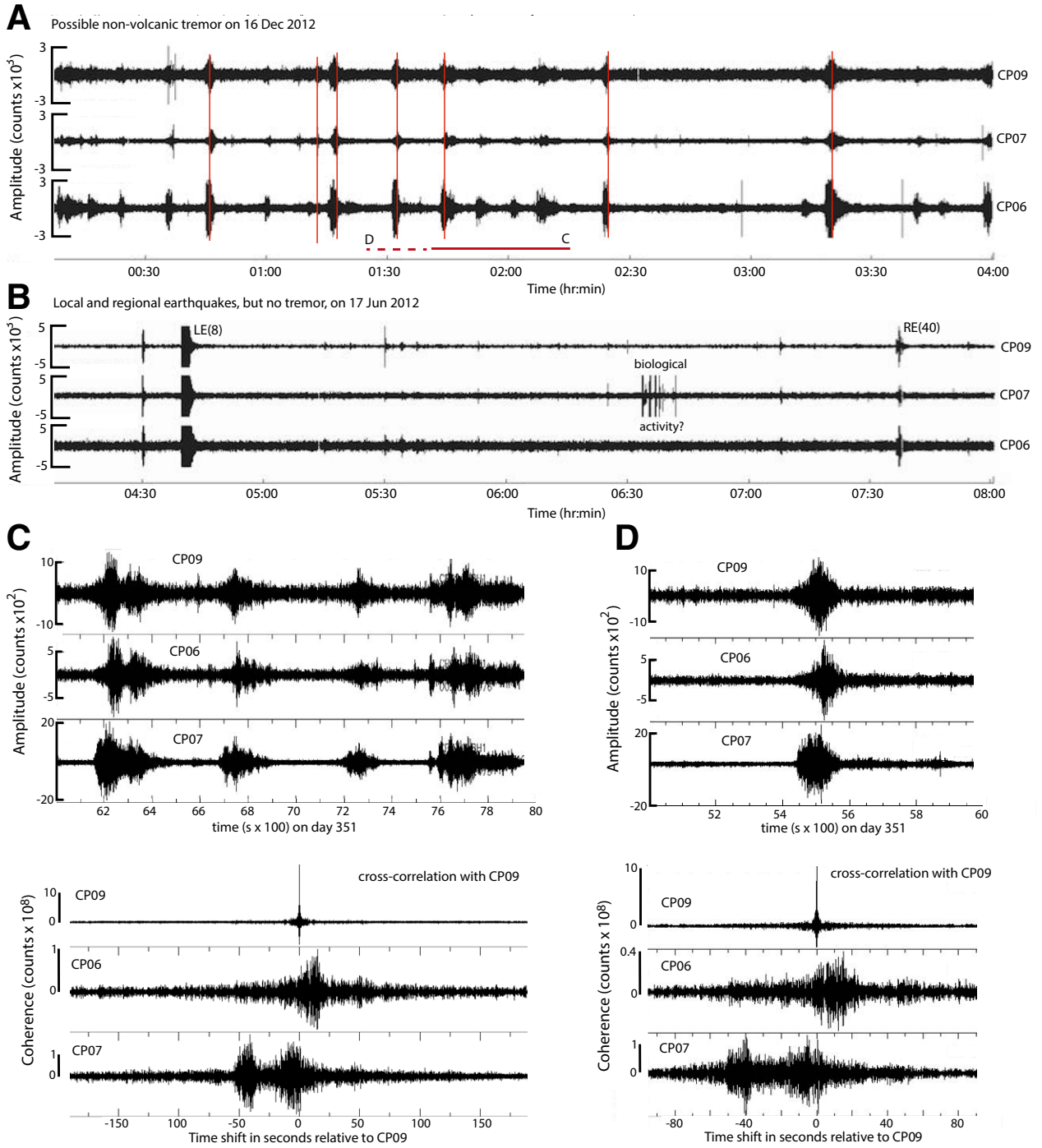

Figure 10. (A) Possible nonvolcanic tremor observed at sites CP06, CP07, and CP09 (see Fig. 1B for location) on 16 December 2012 (Julian day 351). A 4-h-long sample of data on channel BH1 is shown, bandpass filtered at 1–20 Hz. Amplitudes are shown as counts. Data have not been corrected for instrument response; all instruments had the same sensor and recording electronics, but the site response may differ because of soil-structure interaction, as discussed in the text. No data in this time window are clipped, in contrast to the data shown in B. Vertical red lines indicate tremor times detected by the automated tremor detection procedure described in the text. Horizontal solid red line shows the time window displayed in C; horizontal dashed red line shows the time window displayed in D. (B) A 4-h-long sample of data on 17 June 2012, prior to the onset of the transient event shown in Figure 11. Spikes in data from site CP07 may reflect biological activity on or near the ocean-bottom seismometer. Several local events, including a local earthquake (LE) with an S-P time of 8 s and a regional earthquake (RE) with an S-P time of 40 s, are observed in this time window. The local event has a maximum peak-to-peak amplitude of 1,200,000 counts and is clipped on this display; the envelope of the unclipped coda of the local event (not shown) is characterized by a sharp onset and rapid exponential decay, in contrast to the possible tremor shown in A. (C,D) Examples of tremor pulses on 16 December and the cross-correlations used to estimate lag times between stations, as discussed in the text. All times UTC.

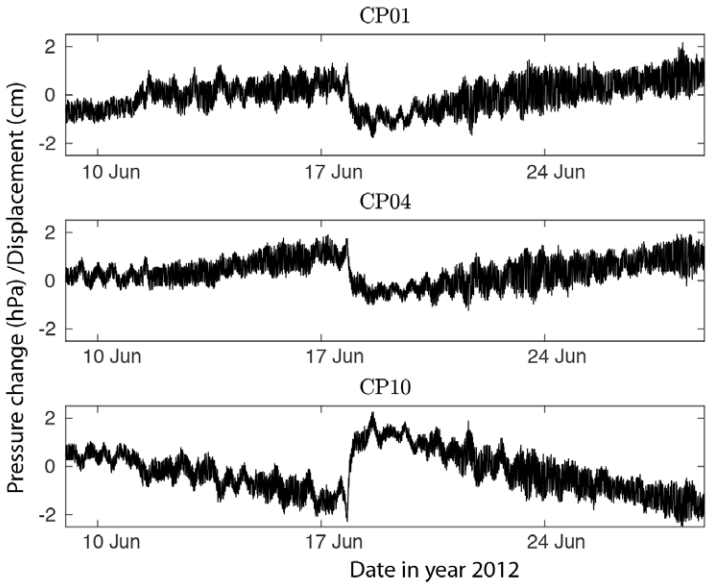

Figure 11. Transient event observed on 17 June 2012 at stations CP1, CP04, and CP10 (see Fig. 1B for location). Data have been processed as described in Section S3 in the Supplemental Material (see footnote 1).

tremor pulses and the general absence of T-phases observed in our data for earthquakes originating in the accretionary prism suggest that these apparent tremor pulses are not T-phases. Moreover, the absence in the CSN catalog of a large earthquake within a few hundred kilometers of the network on 16 December suggests that these events are not aftershocks that look like tremor because of OBS-seafloor coupling resonances. We conclude that it is likely that the ChilePEPPER network recorded nonvolcanic tremor originating in the forearc on 16 December, although we cannot rule out the possibility that some of the pulses detected are due to T-phases from earthquakes. We include these inconclusive results here both as a tantalizing suggestion and a cautionary note. Reliable detection of offshore tremor likely requires both close spacing of stations to detect tremor located within the network and a large aperture to rule out T-phases.

Seafloor Deformation Transients

Slow slip near the deformation front updip of the main slip patch after large earthquakes has been noted in several subduction zones, most notably after the 2005 Nias-Simeulue earthquake (Sumatra, Indonesia), where continuous GPS on islands overlying the outer wedge captured the outer-wedge deformation (Hsu et al., 2006). Shallow slow slip beneath the offshore accretionary prism that was not preceded by a megathrust earthquake downdip has been detected on APGs in the Hikurangi subduction zone (Wallace et al., 2016).

To evaluate whether slow slip events with periods of days to weeks occurred during the post–Maule earthquake deployment, the APG data were processed through a sequence of steps described in Section S3 (footnote 1), which included deterministic removal of the tides (Egbert and Erofeeva, 2002), removal of a long-period drift signal, and reduction of noise using principal component analysis (Dong et al., 2006). This procedure resulted in detection of three episodes of possible transient deformation on 10 May and 17 June 2012 and on 5 January 2013. The processed time series for the largest event (event B) is shown in Figure 11, and the approximate duration and offset observed at each instrument are given in Table 4. The 17 June 2012 transient lasted <24 h, with most of the displacement occurring within 4 h. Subsidence occurred at sites CP01 and CP04 and uplift occurred at site CP10. The pattern of uplift and subsidence is different for the three events, suggesting shallow-rooted deformation of the seafloor.

The second and third transients show a temporal correlation with times of relatively high seismicity (Fig. 9), although in the first case the transient precedes the seismicity, and in the second case the transient follows the seismicity. In both cases, Table S1 (footnote 1) indicates that the earthquakes responsible for the peaks in Figure 9 were small (locations based on four to five observations) and located near the ChilePEPPER network. In contrast, the seismicity peak on 21 November was due to events located well to the north of the network. Although the seismicity peak on 15 September was located near the

TABLE 4. DATE AND DURATION OF THE DETECTED TRANSIENTS IN THE VERTICAL DISPLACEMENT TIME SERIES

	Date	Time of onset (UTC)	Duration	Amplitude Site CP01 (cm)	Amplitude Site CP04 (cm)	Amplitude Site CP10 (cm)
Event A	10 May 2012	23:05	Instantaneous	−1.06 ± 0.01	0.66 ± 0.01	0.32 ± 0.01
Event B	17 Jun 2012	19:40	~1 day	−1.65 ± 0.003	−1.67 ± 0.01	2.95 ± 0.003
Event C	05 Jan 2013	10:00	Two events ~5 days apart	0.85, 0.15	−1.95, −0.35	0.9, 0.30

Notes: Event C is actually two short transients ~5 days apart; the offset during each transient is listed, separated by a comma. See Figure 1B for site locations.

network, no transient was detected around that time. Possible explanations for these transients will be discussed in the concluding section of the paper, which integrates the various observations reported here with the structural framework derived from swath bathymetry and high-resolution multichannel seismic (MCS) data, which are discussed in detail by Tréhu et al. (2019).

Very Low Frequency (VLF) Earthquakes

In 2002, a new class of seismic signals was discovered in the accretionary wedge adjacent to the Nankai Trough offshore Japan (Ishihara, 2003). These events are characterized by peak energy at periods of 10–100 s and little short-period energy and are referred to as VLF (very low frequency) earthquakes. Because of the dearth of high-frequency energy, these events are generally not detected by detection algorithms optimized to find high-frequency events. The spatial occurrence of these events typically overlaps documented aftershock areas in the Nankai Trough, and the unusual properties of these events have been attributed to release of fluid overpressure through fluid expulsion along reverse faults within the accretionary wedge (Obara and Ito, 2005). One of the objectives of ChilePEPPER was to determine whether VLF events were occurring in the accretionary wedge updip as a response to anticipated increased pore pressure in the accretionary wedge induced by slip further downdip during the Maule earthquake.

The APG data from sites CP01, CP04, and CP10 were bandpassed at 0.003–0.07 Hz and visually scanned on all instruments. Forty-three (43) episodes of low-frequency energy were noted (Table S3 [footnote 1]). The times of these events were then compared to times and locations of large seismic events in the U.S. Geological Survey ComCat catalog. All but one of the events corresponded to the expected arrival times of Rayleigh waves. The waveform of the single event that could not be correlated with the catalog was similar to the other interpreted Rayleigh waves, suggesting that it also was a Rayleigh wave from a distant earthquake. We conclude that at most one VLF event (but likely none) large enough to be detected above the background noise level occurred in the vicinity of the ChilePEPPER network during its deployment. Although no VLF events were observed, the ChilePEPPER APG network clearly recorded the tsunami generated by the 2012 Haida Gwaii earthquake (British Columbia, Canada), which generated coherent signals with a primary period of ~20 min (0.0008 Hz) and a peak-to-peak amplitude of ~80 Pa (~8 mm) on the APGs (Fig. S4 [footnote 1]), illustrating the sensitivity of the APGs to very small pressure changes at time scales intermediate between those detected by seismology and geodesy.

Fluid Flow Measurements

According to the dynamic wedge theory of Wang and Hu (2006), stress should increase in the outer accretionary wedge after a great earthquake if the plate boundary beneath the outer wedge is velocity strengthening and slip is arrested downdip of the trench during the main shock. The increased stress should increase pore-fluid pressure within the wedge and induce fluid flow through the sediment-water interface. Slow slip episodes on the plate boundary should also result in pulses of fluid flow. In the Nankai Trough, gradual pore-pressure changes at the toe of the wedge suggest that pore-pressure re-equilibration may take >60 yr (Davis et al., 2013). CAT flow meters designed to detect very low rates of flow into or out of the seafloor (Tryon et al., 2001) were deployed next to OBSs on the outer wedge offshore Costa Rica and recorded oscillating flow of 0.2–1 cm/yr into and out of the seafloor. This flow was correlated with increases in seismic noise (Brown et al., 2005). Modeling suggests that the flow was driven by an episode of localized slow slip on the plate boundary (LaBonte et al., 2009).

For ChilePEPPER, CAT flow meters were integrated into the OBS packages by using the OBS anchor as the collection chamber and attaching the meter to the side of the OBS (Tréhu and Tryon, 2012). The data show that settling of the instruments into the sediments took several months and varied considerably from site to site, yielding in situ records lasting 2–6 months. Once equilibration had been achieved, in situ flow rates were <±0.01 cm/yr (Fig. S5.1 [footnote 1]), and no significant temporal variation was detected. These flow rates are two to three orders of magnitude smaller than rates observed on the Costa Rican margin (Brown et al., 2005, LaBonte et al., 2009) and approach the detection limit of the CAT flow meters. It is difficult to evaluate the significance of this result because of uncertainty about how well the collection chamber was coupled to the seafloor with this instrument configuration.

DISCUSSION

Figure 12A shows the locations of earthquakes in our catalog overlain on structural features of the accretionary prism interpreted from the high-resolution MCS data (Tréhu et al., 2019). As in Figure 5, open circles represent earthquakes located with four or five phases, and filled circles represent earthquakes located with six or more phases. Magenta dots are considered reliable; orange dots are earthquakes for which the epicenters derived from ChilePEPPER data are likely biased to the south, as discussed above. The three APGs on which transients were observed are indicated by yellow triangles outlined in black, and the three seismometers that were used to detect tremor are shown by white triangles outlined in black. Two APGs and one seismometer, outlined in yellow or white, respectively, and filled with gray, were affected by instrumentation problems; although they may have intermittently provided arrival times used for hypocenter locations, they were not used for the tremor and transient analyses. Figure 12B shows hypocenters based on six or more phase picks and at latitudes between 34.8°S and 34.5°S overlain on the velocity model of Moscoso et al. (2011).

One of the more surprising results from the MCS data acquired during ChilePEPPER was an abrupt transition from subduction of nearly all sediment

on the incoming plate at the deformation front south of 34.42°S to accretion of nearly all sediment to the north (Tréhu et al., 2019). This transition in the structure at the deformation front is correlated with a change in the morphology of the active accretionary prism (shown by a magenta line in Fig. 12A) that extends to the boundary between the active prism and continental backstop. Tréhu et al. (2019) argued that this change in deformation front structure cannot be explained by changes in the trench sediment and attributed it to a history of subduction of topographic roughness. They concluded that the abrupt downward step in the plate boundary at this transition affected both the up-dip and along-strike propagation of slip during the Maule earthquake. Both of these outer-prism segments were quiet during the ChilePEPPER deployment, with only a few epicenters based on fewer than six arrival-time readings located within the active accretionary prism in either segment.

The MCS data also indicate that the boundary between the active wedge and the continental basement in this region is a complex zone marked by transpressional structures near the seafloor immediately north and south of the ChilePEPPER network. These are indicated by the blue lines in Figure 12A, which are solid where flower structures are imaged on MCS data and dashed where transpressional ridges are inferred based on bathymetry. The ChilePEPPER network was deployed in a region where the transpressional ridges are not observed. The MCS data suggest that this region is characterized by a pull-apart basin (labeled PAB in Figs. 12A and 12B) formed in response to an extensional stepover in a dominantly right-lateral transpressional shear zone that follows the boundary between the active accretionary prism and the continental framework. Fault mechanisms from first motions for the three largest events of the 15 September 2012 earthquake sequence are roughly consistent with this tectonic setting. Landward of this shear zone, the depth to the paleo-accretionary rocks that comprise the continental basement in this region varies significantly along strike. An uplifted basement dome is present immediately east of the network (labeled DBU in Fig. 12A). The cluster of earthquakes recorded on 15 September 2012, which are among the largest and best located in our catalog, occurred on the boundary between the active accretionary prism and the continental basement as defined by a strong lateral gradient in velocity. Other earthquakes are scattered over a range of depths landward of this boundary or in the subducting crust (with a few additional earthquakes in the upper mantle below 25 km, which are not shown here).

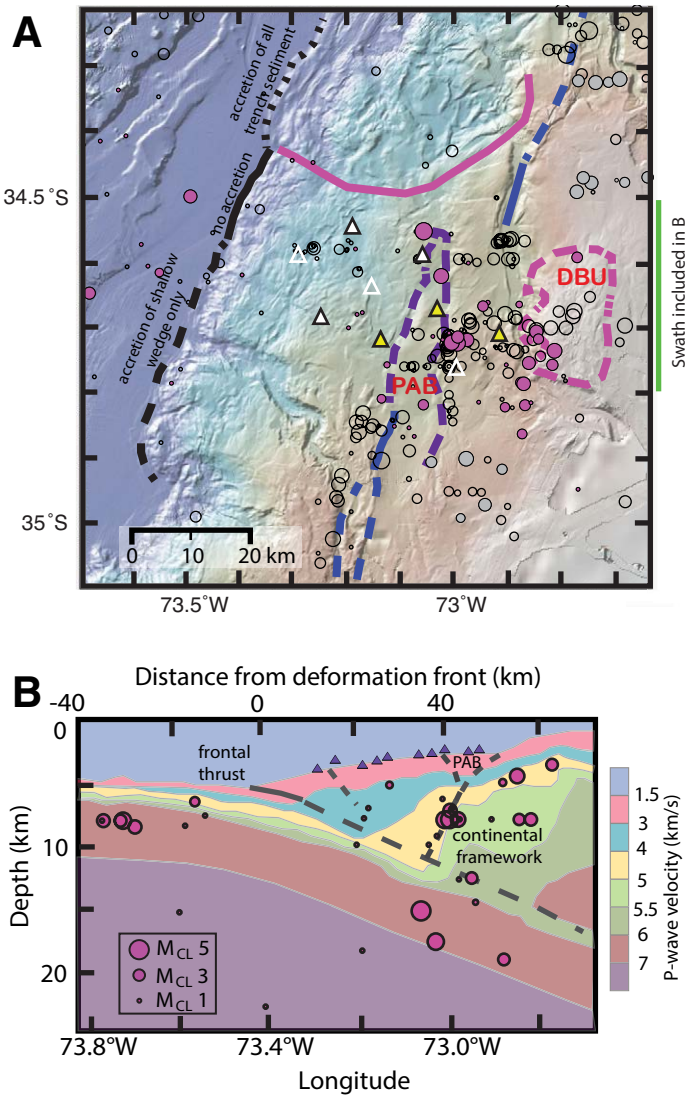

Figure 12. (A) Earthquakes located using data from the ChilePEPPER network. Open circles are events located with fewer than six arrival time picks; magenta and grey filled circles are located with six to 11 arrival-time picks. Grey circles are likely mislocated with a bias toward the network for reasons discussed in the text. Circle diameters are proportional to coda magnitude determined as discussed in Section S1 in the Supplemental Material (see footnote 1). See B for scale. Triangles are ChilePEPPER ocean-bottom seismometer locations. White indicates seismometers used for tremor analysis; yellow indicates absolute pressure gauges used for transient analysis; all stations were used to locate earthquakes. Blue lines indicate transpressional structures near the seafloor (solid line for flower structures, dashed line for transpressional ridges inferred from bathymetry). Magenta line delimits a region of disrupted topography interpreted to indicate subduction of a large topographic feature at ~2 Ma (Tréhu et al., 2019). PAB—pull-apart basin; DBU—domal basement uplift. See text for further discussion. (B) Depth below sea level versus longitude for earthquakes (magenta filled circles) with latitude between 34.5°S and 34.8°S and located using at least six arrival-time picks, compared to the velocity model of Moscoso et al. (2011). Long dashed line is the plate boundary interpreted by Moscoso et al. (2011), modified to incorporate results of Tréhu et al. (2019) near the deformation front (solid line). Purple triangles are the projected location of the ChilePEPPER instruments. Short dashed lines are upper plate structures discussed by Tréhu et al. (2019).

We interpret the three transients detected on the APGs to represent adjustments in response to motion on the boundary between the active prism and the continental basement. The detailed nature of the deformation resulting in these observations is poorly constrained. They could reflect slumping of near-surface topography generated in response to faulting at greater depth or a response to motion on shallow faults that reach the seafloor. Given the complexity of the local structure, the variability in the observations, and the expected anelastic behavior of the sediments, we did not attempt to model these results. Given the increasing interest in seafloor geodesy and the small number of results reported from seafloor APGs, we nonetheless think they merit being reported as additional evidence documenting the promise of APGs as a tool for seafloor geodesy as well as evidence for continuing tectonic activity on the boundary between the active accretionary wedge and the continental basement.

Many pulses of energy in the 2–8 Hz range that resemble nonvolcanic tremor were detected throughout the deployment, but techniques developed for locating tremor on land were not successful at locating the source of the tremor. Detailed examination of the lag times of tremor pulses during the 16 December "swarm" indicates a source located in either the ocean or the shallow forearc wedge several tens of kilometers south or southeast of the ChilePEPPER network, although the precision with which lag times can be picked precludes a precise determination of the source location. Based on the observation that most earthquakes that generated T-phases during the ChilePEPPER deployment were located seaward of the deformation front, an apparent source landward of the deformation front suggests that these tremor pulses may have a shallow subseafloor source. More detailed analysis of the azimuth of approach and apparent velocity of tremor pulses throughout the experiment is underway. These tantalizing results (as well as the transients observed on the APGs) illustrate the need for large-aperture networks with small interstation spacing, requiring larger numbers of seafloor instruments.

CONCLUSIONS

We have located earthquakes with S-P times <17 s (i.e., within ~125 km of the network), with 34 earthquakes located with at least six phase picks, RMS residual <0.5 s, and the closest station within 16 km of the epicenter. Most of the seismicity occurred either near the boundary between the inner and outer wedge or in the outer rise of the subducting plate seaward of the deformation front. For ~50% of the outer-rise earthquakes, the P- and S-wave arrivals were followed by a distinctive T-phase arrival traveling in the ocean. T-phases were rare for earthquakes located landward of the deformation front. Very few earthquakes, and none located with hypocenters deemed "reliable," were located within the active accretionary wedge or on the underlying plate boundary. Comparison of hypocenters for earthquakes within the ChilePEPPER network with hypocenters for the same events reported by onshore catalogs suggests that depths determined with only onshore data and using velocity models appropriate for the coastal region are systematically overestimated.

Application of techniques used to detect nonvolcanic tremor resulted in identification of many potential tremor events. For offshore events recorded on offshore seismometers, distinguishing between nonvolcanic tremor from sources beneath the seafloor and T-phases from tectonic earthquakes is challenging with a small-aperture network. Because of uncertainties in defining the lag time of these arrivals between stations in the network, we were not able to locate the source of the nonvolcanic tremor or conclusively rule out the possibility of T-phases. Close examination of the lag times across the network on the day with the largest number of apparent tremor events indicates that the source of the observations was south or southeast of the network, either along the boundary between the accretionary prism and the continental framework or within the continental framework. The maximum velocities compatible with the observed lags suggest that the source depths were within either the ocean or near-seafloor sediments. In addition to T-phases, P and S waves from earthquakes that reverberate in the uppermost layer of very low-velocity sediments on the seafloor can resemble nonvolcanic tremor. Misidentification as tremor of aftershocks that trigger these reverberations is the likely explanation for an episode of apparent triggered tremor following a M 6 earthquake near the Chile-Argentina border ~270 km from the network.

Analysis of the APG data resulted in several important observations. First, although the APGs were not a good sensor for detecting small, local earthquakes because of a rapid increase in background noise level at frequencies <2 Hz, they did serve as strong-motion instruments for larger, local earthquakes that saturated the seismometers. At longer periods, they proved to be very sensitive, and were used to detect several transient events with a duration of several hours to a few days on instruments that straddled the boundary between the active prism and the continental framework. Because the polarity of the transients differs between stations and between events, we conclude that they represent readjustments of forearc basin sediments in response to tectonic motion along a buried shear zone.

No VLF earthquakes or fluid flow into or out of the seafloor were detected, suggesting that if pore pressures in the outer accretionary prism were elevated in response to the Maule earthquake, release of pressure by flow through the seafloor was below the detection threshold of our instruments.

In spite of limitations due to the small number of stations, the results demonstrate the value of deploying networks of seismometers and APGs in the ocean after major earthquakes in order to document postseismic deformation and understand interplate dynamics. While close instrument spacing was required to obtain good constraints on the depth of earthquakes within the network as well as for detecting tremor and spatially varying transients, all of these measurements would have benefited from a larger-aperture network; however, ten instruments equipped with broadband seismometers, APGs, and flow meters were available for deployment on short notice, resulting in a tradeoff between spacing and aperture. The results underscore the need for large numbers of OBSs capable of measuring seafloor deformation over a wide range of time scales.

ACKNOWLEDGMENTS

We thank the captains and crews of the R/V *Melville* and R/V *Point Sur* and the staff of the U.S. Ocean Bottom Instrument Facility at Lamont-Doherty Earth Observatory for their support for this project. Funding was provided by U.S. National Science Foundation grants OCE1130013 to Oregon State University (OSU; A.M. Tréhu) and OCE1129574 to Scripps Institution of Oceanography (SIO; M.D. Tryon). Support for J. Mieres Madrid to visit OSU and SIO was provided by CONICYT/FONDECYT grant 11170047 (Un. Chile; J. Ruiz and E. Contreras-Reyes). The paper benefitted greatly from thoughtful and probing reviews from Guest Associate Editor Laura Wallace and two annonymous reviewers. All OBS data are available from the IRIS Data Management Center (http://ds.iris.edu/). Underway data and cruise reports are available from the Rolling Deck to Repository (https://www.rvdata.us/).

REFERENCES CITED

Agurto, H., Rietbrock, A., Ryder, I., and Miller, M., 2012, Seismic-afterslip characterization of the 2010 M_w 8.8 Maule, Chile, earthquake based on moment tensor inversion: Geophysical Research Letters, v. 39, L20303, https://doi.org/10.1029/2012GL053434.

Angermann, D., Klotz, J., and Reigber, C., 1999, Space-geodetic estimation of the Nazca–South America Euler vector: Earth and Planetary Science Letters, v. 171, p. 329–334, https://doi.org/10.1016/S0012-821X(99)00173-9.

Balanche, A., Guennou, C., Goslin, J., and Mazoyer, C., 2009, Generation of hydroacoustic signals by oceanic earthquakes: A mechanical model: Geophysical Journal International, v. 177, p. 476–480, https://doi.org/10.1111/j.1365-246X.2009.04146.x.

Bangs, N.L., and Cande, S.C., 1997, Episodic development of a convergent margin inferred from structures and processes along the southern Chile margin: Tectonics, v. 16, p. 489–503, https://doi.org/10.1029/97TC00494.

Blackman, D.K., Nishimura, C.E., and Orcutt, J.A., 2000, Seismoacoustic recordings of a spreading episode on the Mohns Ridge: Journal of Geophysical Research, v. 105, p. 10,961–10,973, https://doi.org/10.1029/2000JB900011.

Bohnenstiehl, D.R., Tolstoy, M., Dziak, R.P., Fox, C.G., and Smith, D.K., and 2002, Aftershock sequences in the mid-ocean ridge environment: An analysis using hydroacoustic data: Tectonophysics, v. 354, p. 49–70, https://doi.org/10.1016/S0040-1951(02)00289-5.

Brown, K.M., Tryon, M.D., DeShon, H.R., Dorman, L.M., and Schwartz, S.Y., 2005, Correlated transient fluid pulsing and seismic tremor in the Costa Rica subduction zone: Earth and Planetary Science Letters, v. 238, p. 189–203, https://doi.org/10.1016/j.epsl.2005.06.055.

Campos, J., Hatzfeld, D., Madariaga, R., Lopez, G., Kausel, E., Zollo, A., Iannacone, R., Fromm, R., Barrientos, S., and Lyon-Caen, H., 2002, A seismological study of the 1835 seismic gap in south-central Chile: Physics of the Earth and Planetary Interiors, v. 132, p. 177–195, https://doi.org/10.1016/S0031-9201(02)00051-1.

Contardo, X., Cembrano, J., Jensen, A., and Díaz-Naveas, J., 2008, Tectono-sedimentary evolution of marine slope basins in the Chilean forearc (33°30′–36°50′S): Insights into their link with the subduction process: Tectonophysics, v. 459, p. 206–218, https://doi.org/10.1016/j.tecto.2007.12.014.

Contreras-Reyes, E., and Carrizo, D., 2011, Control of high oceanic features and subduction channel on earthquake ruptures along the Chile–Peru subduction zone: Physics of the Earth and Planetary Interiors, v. 186, p. 49–58, https://doi.org/10.1016/j.pepi.2011.03.002.

Contreras-Reyes, E., and Osses, A., 2010, Lithospheric flexure modeling seaward of the Chile trench: Implications for oceanic plate weakening in the trench outer rise region: Geophysical Journal International, v. 182, p. 97–112, https://doi.org/10.1111/j.1365-246X.2010.04629.x.

Contreras-Reyes, E., Flueh, E.R., and Grevemeyer, I., 2010, Tectonic control on sediment accretion and subduction off south central Chile: Implications for coseismic rupture processes of the 1960 and 2010 megathrust earthquakes: Tectonics, v. 29, TC6018, https://doi.org/10.1029/2010TC002734.

Contreras-Reyes, E., Maksymowicz, A., Lange, D., Grevemeyer, I., Munoz-Linford, P., and Moscoso, E., 2017, On the relationship between structure, morphology and large coseismic slip: A case study of the Mw 8.8 Maule, Chile 2010 earthquake: Earth and Planetary Science Letters, v. 478, p. 27–39, https://doi.org/10.1016/j.epsl.2017.08.028.

Cubas, N., Avouac, J.P., Souloumiac, P., and Leroy, Y.M., 2013a, Megathrust friction determined from mechanical analysis of the forearc in the Maule earthquake area: Earth and Planetary Science Letters, v. 381, p. 92–103, https://doi.org/10.1016/j.epsl.2013.07.037.

Cubas, N., Avouac, J.P., Leroy, Y.M., and Pons, A., 2013b, Low friction on the high slip patch of the 2011 Mw 9.0 Tohoku-Oki earthquake required from the wedge structure and extensional splay faults: Geophysical Research Letters, v. 40, p. 4231–4237, http://doi.org/10.1002/grl.50682.

Czoski, P.A., Tréhu, A.M., Williams, M.C., Dziak, R.P., and Embley, R.W., 2012, The August and October 2008 earthquake swarms on the Explorer/Pacific plate boundary [abs.]: Seismological Research Letters, v. 83, p. 425–426.

Davis, E.E., Kinoshita, M., Wang, K., Asano, Y., Ito, Y., and Becker, K., 2013, Episodic deformation and inferred slow slip at the Nankai subduction zone during the first decade of CORK borehole pressure and VLFE monitoring: Earth and Planetary Science Letters, v. 368, p. 110–118, https://doi.org/10.1016/j.epsl.2013.03.009.

de Groot-Hedlin, C.D., and Orcutt, J.D., 2001, Excitation of T-phases by seafloor scattering: Journal of the Acoustical Society of America, v. 109, p. 1944–1954, https://doi.org/10.1121/1.1361057.

Delouis, B., Nocquet, J.-M., and Vallee, M., 2010, Slip distribution of the February 27, 2010 Mw = 8.8 Maule earthquake, central Chile, from static and high-rate GPS, InSAR, and broadband seismic data: Geophysical Research Letters, v. 37, L17305, https://doi.org/10.1029/2010GL043899.

de Moor, A., 2015, Local seismicity recorded by ChilePEPPER: Implications for dynamic accretionary prism response and long-term prism evolution [M.S. thesis]: Corvallis, Oregon State University, 79 p., https://ir.library.oregonstate.edu/concern/graduate_thesis_or_dissertations/00000354x.

Dong, D., Fang, P., Bock, Y., Webb, F., Prawirodirdjo, L., Kedar, S., and Jamason, P., 2006, Spatiotemporal filtering using principal component analysis and Karhunen-Loeve expansion approaches for regional GPS network analysis: Journal of Geophysical Research, v. 111, B03405, https://doi.org/10.1029/2005JB003806.

Dziak, R.P., 2001, Empirical relationship of T-wave energy and fault parameters of northeast Pacific Ocean earthquakes: Geophysical Research Letters, v. 28, p. 2537–2540, https://doi.org/10.1029/2001GL012939.

Dziak, R.P., Fox, C.G., and Schreiner, A.E., 1995, The June-July 1993 seismo-acoustic event at CoAxial segment, Juan de Fuca Ridge: Evidence for a lateral dike injection: Geophysical Research Letters, v. 22, p. 135–138, https://doi.org/10.1029/94GL01857.

Dziak, R.P., Bohnenstiehl, D.R., Matsumoto, H., Fox, C.G., Smith, D.K., Tolstoy, M., Lau, T.-K., Haxel, J.H., and Fowler, M.J., 2004, P- and T-wave detection thresholds, *Pn* velocity estimate, and detection of lower mantle and core P-waves on ocean sound-channel hydrophones at the Mid-Atlantic Ridge: Bulletin of the Seismological Society of America, v. 94, p. 665–677, https://doi.org/10.1785/0120030156.

Egbert, G.D., and Erofeeva, S.Y., 2002, Efficient inverse modeling of barotropic ocean tides: Journal of Atmospheric and Oceanic Technology, v. 19, p. 183–204, https://doi.org/10.1175/1520-0426(2002)019<0183:EIMOBO>2.0.CO;2.

Fagereng, Å., 2011, Wedge geometry, mechanical strength, and interseismic coupling of the Hikurangi subduction thrust, New Zealand: Tectonophysics, v. 507, p. 26–30, https://doi.org/10.1016/j.tecto.2011.05.004.

Forsyth, D.W., Yang, Y., Mangriotis, M.-D., and Shen, Y., 2003, Coupled seismic slip on adjacent oceanic transforms: Geophysical Research Letters, v. 30, 1618, https://doi.org/10.1029/2002GL016454.

Hashimoto, Y., Tobin, H.J., Knuth, M., and Harada, A., 2011, Data report: Compressional and shear wave velocity measurements on sediment in the hanging wall and footwall of megasplay fault, NanTroSEIZE Stage 1, *in* Kinoshita, M., Tobin, H., Ashi, J., Kimura, G., Lallemant, S., Screaton, E.J., Curewitz, D., Masago, H., Moe, K.T., and the Expedition 314/315/316 Scientists, Proceedings of the Integrated Ocean Drilling Program, Volume 314/315/316: Washington, D.C., Integrated Ocean Drilling Program Management International, Inc., https://doi.org/10.2204/iodp.proc.314315316.217.2011.

Hayes, G.P., Wald, D.J., and Johnson, R.L., 2012, Slab1.0: A new three-dimensional model of global subduction interface geometry: Journal of Geophysical Research, v. 117, https://doi.org/10.1029/2011JB008524.

Hayes, G.P., Bergman, E., Johnson, K.L., Benz, H.M., Brown, L., and Meltzer, A.S., 2013, Seismotectonic framework of the February 27, 2010 M_w 8.8 Maule, Chile earthquake sequence: Geophysical Journal International, v. 195, p. 1034–1051, https://doi.org/10.1093/gji/ggt238.

Hicks, S.P., Rietbrock, A., Ryder, I.M.A., Lee, C.-S., and Miller, M., 2014, Anatomy of a megathrust: The 2010 M8.8 Maule, Chile earthquake rupture zone imaged using seismic tomography: Earth and Planetary Science Letters, v. 405, p. 142–155, https://doi.org/10.1016/j.epsl.2014.08.028.

Hsu, Y.J., Simons, M., Avouac, J.P., Galetzka, J., Sieh, K., Chlieh, M., Natawidjaja, D., Prawirodirdjo, L., and Bock, Y., 2006, Frictional afterslip following the 2005 Nias-Simeulue earthquake, Sumatra: Science, v. 312, p. 1921–1926, https://doi.org/10.1126/science.1126960.

Ishihara, Y., 2003, Major existence of very low frequency earthquakes in background seismicity along subduction zone of south-western Japan: Eos (Transactions, American Geophysical Union), v. 84, Fall Meeting Suppl., Abstract S41C-0107.

Kodaira, S., No, T., Nakamura, Y., Fujiwara, T., Kaiho, Y., Miura, S., Takahashi, N., Kaneda, Y., and Taira, A., 2012, Coseismic fault rupture at the trench axis during the 2011 Tohoku-oki earthquake: Nature Geoscience, v. 5, p. 646–650, https://doi.org/10.1038/ngeo1547.

Kukowski, N., and Oncken, O., 2006, Subduction erosion: The "normal" mode of fore-arc material transfer along the Chilean margin?, *in* Oncken, O., Chong, G., Franz, G., Giese, P., Götze, H.-J., Ramos, V.A., Strecker, M.R., and Wigger, P., eds., The Andes: Active Subduction Orogeny: Berlin, Springer, Frontiers in Earth Sciences, v. 3, p. 217–236, https://doi.org/10.1007/978-3-540-48684-8_10.

LaBonte, A.L., Brown, K.M., and Fialko, Y., 2009, Hydrologic detection and finite element modeling of a slow slip event in the Costa Rica prism toe: Journal of Geophysical Research, v. 114, B00A02, https://doi.org/10.1029/2008JB005806.

Lallemand, S.E., Schnürle, P., and Malavieille, J., 1994, Coulomb theory applied to accretionary and nonaccretionary wedges: Possible causes for tectonic erosion and/or frontal accretion: Journal of Geophysical Research, v. 99, p. 12,033–12,055, https://doi.org/10.1029/94JB00124.

Lange, D., Tilmann, F., Barrientos, S.E., Contreras- Reyes, E., Methe, P., Moreno, M., Heit, B., Bernard, P., Vilotte, J.-P., and Beck, S., 2012, Aftershock seismicity of the 27 February 2010 Mw 8.8 Maule earthquake rupture zone: Earth and Planetary Science Letters, v. 317-318, p. 413-425, https://doi.org/10.1016/j.epsl.2011.11.034.

Lay, T., Ammon, C.J., Kanamori, H., Koper, K.D., Sufri, O., and Hutko, A.R., 2010, Teleseismic inversion for rupture process of the 27 February 2010 Chile (M_w 8.8) earthquake: Geophysical Research Letters, v. 37, L13301, https://doi.org/10.1029/2010GL043379.

Lee, W.H., and Lahr, J.C., 1975, HYPO71 (revised): A computer program for determining hypocenter, magnitude, and first motion pattern of local earthquakes: U.S. Geological Survey Open-File Report 75-311, 113 p., https://doi.org/10.3133/ofr75311.

Lieser, K., Grevemeyer, I., Lange, D., Flueh, E., Tilmann, F., and Contreras-Reyes, E., 2014, Splay fault activity revealed by aftershocks of the 2010 M_w 8.8 Maule earthquake, central Chile: Geology, v., 42, p. 823–826, https://doi.org/10.1130/G35848.1.

Lin, Y.-n.N., Sladen, A., Ortega-Culaciati, F., Simons, M., Avouac, J.-P., Fielding, E.J., Brooks, B.A., Bevis, M., Genrich, J., Rietbrock, A., Vigny, C., Smalley, R., and Socquet, A., 2013, Coseismic and postseismic slip associated with the 2010 Maule Earthquake, Chile: Characterizing the Arauco Peninsula barrier effect: Journal of Geophysical Research: Solid Earth, v. 118, p. 3142–3159, https://doi.org/10.1002/jgrb.50207.

Lomnitz, C., 2004, Major earthquakes of Chile: A historical survey, 1535–1960: Seismological Research Letters, v. 75, p. 368–378, https://doi.org/10.1785/gssrl.75.3.368.

Lorito, S., Romano, F., Atzori, S., Tong, X., Avallone, A., McCloskey, J., Cocco, M., Boschi, E., and Piatanesi, A., 2011, Limited overlap between the seismic gap and coseismic slip of the great 2010 Chile earthquake: Nature Geoscience, v. 4, p. 173–177, https://doi.org/10.1038/ngeo1073.

Loveless, J.P., Pritchard, M.E., and Kukowski, N., 2010, Testing mechanisms of subduction zone segmentation and seismogenesis with slip distributions from recent Andean earthquakes: Tectonophysics, v. 495, p. 15–33, https://doi.org/10.1016/j.tecto.2009.05.008.

Maksymowicz, A., Tréhu, A.M., Contreras-Reyes, E., and Ruiz, S., 2015, Density-depth model of the continental wedge at the maximum slip segment of the Maule Mw8.8 megathrust earthquake: Earth and Planetary Science Letters, v. 409, p. 265–277, https://doi.org/10.1016/j.epsl.2014.11.005.

Maksymowicz, A., Chadwell, C.D., Ruiz, J., Tréhu, A.M., Contreras-Reyes, E., Weinrebe, W., Díaz-Naveas, J., Gibson, J.C., Lonsdale, P., and Tryon, M.D., 2017, Coseismic seafloor deformation in the trench region during the Mw 8.8 Maule megathrust earthquake: Scientific Reports, v. 7, 45918, https://doi.org/10.1038/srep45918.

Mix, A.C., Tiedemann, R., Blum, P., et al., 2003, Proceedings of the Ocean Drilling Program, Initial Reports, Volume 202: College Station, Texas, Ocean Drilling Program, https://doi.org/10.2973/odp.proc.ir.202.2003.

Moreno, M., Rosenau, M., and Oncken, O., 2010, 2010 Maule earthquake slip correlates with pre-seismic locking of Andean subduction zone: Nature, v. 467, p. 198–202, https://doi.org/10.1038/nature09349.

Moreno, M., Melnick, D., Rosenau, M., Baez, J., Klotz, J., Oncken, O., Tassara, A., Chen, J., Bataille, K., Bevis, M., Soquet, A., Bolte, J., Vigny, C., Brooks, B., Ryder, I., Grund, V., Smalley, B., Carrizo, D., Bartsch, M., and Hase, H., 2012, Toward understanding tectonic control on the Mw 8.8 2010 Maule Chile earthquake: Earth and Planetary Science Letters, v. 321–322, p. 152–165, https://doi.org/10.1016/j.epsl.2012.01.006.

Moscoso, E., Grevemeyer, I., Contreras-Reyes, E., Flueh, E.R., Dzierma, Y., Rabbel, W., and Thorwart, M., 2011, Revealing the deep structure and rupture plane of the 2010 Maule, Chile earthquake (Mw = 8.8) using wide angle seismic data: Earth and Planetary Science Letters, v. 307, p. 147–155, https://doi.org/10.1016/j.epsl.2011.04.025.

Nakano, M., Hori, T., Araki, E., Takahashi, N., and Kodaira, S., 2016, Ocean floor networks capture low-frequency earthquake event: Eos (Transactions, American Geophysical Union), v. 97, https://doi.org/10.1029/2016EO052877.

Obara, K., and Ito, Y., 2005, Very low frequency earthquakes excited by the 2004 off the Kii peninsula earthquakes: A dynamic deformation process in the large accretionary prism: Earth, Planets, and Space, v. 57, p. 321–326, https://doi.org/10.1186/BF03352570.

Poli, P., Maksymowicz, A., and Ruiz, S., 2017, The M_w 8.3 Illapel earthquake (Chile): Preseismic and postseismic activity associated with hydrated slab structures: Geology, v. 45, p. 247–250, https://doi.org/10.1130/G38522.1.

Pollitz, F.F., Brooks, B., Tong, X., Bevis, M.G., Foster, J.H., Bürgmann, R., Smalley, R., Jr., Vigny, C., Socquet, A., Ruegg, J.-C., Campos, J., Barrientos, S., Parra, H., Baez Soto, J.C., Cimbaro, S., and Blanco, M., 2011, Coseismic slip distribution of the February 27, 2010 Mw 8.8 Maule, Chile earthquake: Geophysical Research Letters, v. 38, L09309, https://doi.org/10.1029/2011GL047065.

Rietbrock, A., Ryder, I., Hayes, G., Haberland, C., Comte, D., Roecker, S., and Lyon-Caen, H., 2012, Aftershock seismicity of the 2010 Maule Mw = 8.8, Chile, earthquake: Correlation between co-seismic slip models and aftershock distribution: Geophysical Research Letters, v. 39, L08310, https://doi.org/10.1029/2012GL051308.

Ruegg, J.C., Rudloff, A., Vigny, C., Madariaga, R., de Chabalier, J.B., Campos, J., Kausel, E., Barrientos, S., and Dimitrov, D., 2009, Interseismic strain accumulation measured by GPS in the seismic gap between Constitución and Concepción in Chile: Physics of the Earth and Planetary Interiors, v. 175, p. 78–85, https://doi.org/10.1016/j.pepi.2008.02.015.

Ruff, L.J., 1989, Do trench sediments affect great earthquake occurrence in subduction zones?: Pure and Applied Geophysics, v. 129, p. 263–282, https://doi.org/10.1007/BF00874629.

Ruiz, S., and Madariaga, R., 2018, Historical and recent large megathrust earthquakes in Chile: Tectonophysics, v. 733, p. 37–56, https://doi.org/10.1016/j.tecto.2018.01.015.

Russo, R.M., Beck, S.L., Roecker, S.W., Reusch, A.M., Velasco, A., Ebeling, C., and Bremner, P.M., 2011, EarthScope participates in open data seismic deployment following 2010 Chile earthquake: inSights (EarthScope newsletter), http://www.earthscope.org/articles/open_seismic_data_deployment (accessed August 2019).

Ryan, W.B.F., Carbotte, S.M., Copan, J.O., O'Hara, S., Melkonian, A., Arko, R., Weissel, R.A., Ferrini, V., Goodwillie, A., Nitsche, F., Bonczkowski, J., and Zemsky, R., 2009, Global Multi-Resolution Topography synthesis: Geochemistry Geophysics Geosystems, v. 10, Q03014, https://doi.org/10.1029/2008GC002332.

Sato, M., Ishikawa, T., Ujihara, N., Yoshida, S., Fujita, M., Mochizuki, M., and Asada, A., 2011, Displacement above the hypocenter of the 2011 Tohoku-Oki earthquake: Science, v. 332, p. 1395, https://doi.org/10.1126/science.1207401.

Scholl, D.W., Kirby, S.H., von Huene, R., Ryan, H., Wells, R.E., and Geist, E.L., 2015, Great (≥Mw8.0) megathrust earthquakes and the subduction of excess sediment and bathymetrically smooth seafloor: Geosphere, v. 11, p. 236–265, https://doi.org/10.1130/GES01079.1.

Tong, X., Sandwell, D., Luttrell, K., Brooks, B., Bevis, M., Shimada, M., Foster, J., Smalley, R., Jr., Parra, H., Báez Soto, J.C., Blanco, M., Kendrick, E., Genrich, J., and Caccamise, D.J., II, 2010, The 2010 Maule, Chile earthquake: Downdip rupture limit revealed by space geodesy: Geophysical Research Letters, v. 37, L24311, https://doi.org/10.1029/2010GL045805.

Tréhu, A.M., 1985, Coupling of ocean bottom seismometers to sediment: Results of tests with the U.S. Geological Survey ocean bottom seismometer: Bulletin of the Seismological Society of America, v. 75, p. 271–289.

Tréhu, A., 2013, Cruise report: R/V *Point Sur*, PS1306: https://doi.org/10.7284/903032 (last accessed August 2019).

Tréhu, A., and Tryon, M., 2012, Cruise report: R/V *Melville*, MV1206—The 2010 Maule, Chile Earthquake: Project Evaluating Prism Post-Earthquake Response (Chile-PEPPER), https://doi.org/10.7284/903827 (last accessed August 2019).

Tréhu, A.M., Braunmiller, J., and Davis, E., 2015, Seismicity of the central Cascadia Continental margin near 44.5° N: A decadal view: Seismological Research Letters, v. 86, p. 819–829, https://doi.org/10.1785/0220140207.

Tréhu, A.M., Wilcock, W.S.D., Hilmo, R., Bodin, P., Connolly, J., Roland, E.C., and Braunmiller, J., 2018, The role of the Ocean Observatories Initiative in monitoring the offshore earthquake activity of the Cascadia subduction zone: Oceanography, v. 31, p. 104–113, https://doi.org/10.5670/oceanog.2018.116.

Tréhu, A.M., Hass, B., de Moor, A., Maksymowicz, A., Contreras-Reyes, E., Vera, E., and Tryon, M.D., 2019, Geologic controls on up-dip and along-strike propagation of slip during subduction zone earthquakes from a high-resolution seismic reflection survey across the northern limit of slip during the 2010 Mw 8.8 Maule earthquake, offshore Chile: Geosphere, v. 15, https://doi.org/10.1130/GES02099.1.

Tryon, M., Brown, K., Dorman, L., and Sauter, A., 2001, A new benthic aqueous flux meter for very low to moderate discharge rates: Deep Sea Research Part I: Oceanographic Research Papers, v. 48, p. 2121–2146, https://doi.org/10.1016/S0967-0637(01)00002-4.

Vigny, C., et al., 2011, The 2010 M_w 8.8 Maule megathrust earthquake of central Chile, monitored by GPS: Science, v. 332, p. 1417–1421, https://doi.org/10.1126/science.1204132.

Völker, D., Geersen, J., Contreras-Reyes, E., and Reichert, C., 2013, Sedimentary fill of the Chile Trench (32–46°S): Volumetric distribution and causal factors: Journal of the Geological Society of London, v. 170, p. 723–736, https://doi.org/10.1144/jgs2012-119.

Wallace, L.M., Webb, S.C., Ito, Y., Mochizuki, K., Hino, R., Henrys, S., Schwarz, S.Y., and Sheehan, A.F., 2016, Slow slip near the trench at the Hikurangi subduction zone, New Zealand: Science, v. 352, p. 701–704, https://doi.org/10.1126/science.aaf2349.

Wang, K., and Dixon, T., 2004, "Coupling" semantics and science in earthquake research: Eos (Transactions, American Geophysical Union), v. 85, p. 180, https://doi.org/10.1029/2004EO180005.

Wang, K., and Hu, Y., 2006, Accretionary prisms in subduction earthquake cycles: The theory of dynamic Coulomb wedge: Journal of Geophysical Research, v. 111, B06410, https://doi.org/10.1029/2005JB004094.

Webb, S.C., and Nooner, S.L., 2016, High-resolution seafloor absolute pressure gauge measurements using a better counting method: Journal of Atmospheric and Oceanic Technology, v. 33, p. 1859–1874, https://doi.org/10.1175/JTECH-D-15-0114.1.

Wech, A.G., Sheehan, A.F., Boese, C.M., Townend, J., Stern, T.A., and Collins, J.A., 2013, Tectonic tremor recorded by ocean bottom seismometers: Seismological Research Letters, v. 84, p. 752–758, https://doi.org/10.1785/0220120184.

Wech, A., Tepp, G., Lyons, J., and Haney, M., 2018, Using earthquakes, T waves, and infrasound to investigate the eruption of Bogoslof Vocano, Alaska: Geophysical Research Letters, v. 45, p. 6918–16925, https://doi.org/10.1029/2018GL078457.

Williams, M.C., Tréhu, A.M., and Braunmiller, J., 2011, Seismicity at the Cascadia plate boundary beneath the Oregon continental shelf: Bulletin of the Seismological Society of America, v. 101, p. 940–950, https://doi.org/10.1785/0120100198.

Ye, L., Lay, T., Kanamori, H., and Rivera, L., 2016, Rupture characteristics of major and great (M_w 7.0) megathrust earthquakes from 1990 to 2015: 1. Source parameter scaling relationships: Journal of Geophysical Research: Solid Earth, v. 121, p. 826–844, https://doi.org/10.1002/2015JB012426.

Yue, H., Lay, T., Rivera, L., An, C., Vigny, C., Tong, X., and Báez Soto, J.C., 2014, Localized fault slip to the trench in the 2010 Maule, Chile M_w = 8.8 earthquake from joint inversion of high-rate GPS, teleseismic body waves, InSAR, campaign GPS, and tsunami observations: Journal of Geophysical Research: Solid Earth, v. 119, p. 7786–7804, https://doi.org/10.1002/2014JB011340.